International Journal of Coal Geology 310 (2025) 104869

Contents lists available at ScienceDirect

International Journal of Coal Geology

journal homepage: www.elsevier.com/locate/coal

Unraveling hiatuses in black shales: Mechanisms and implications from the Lower Silurian Longmaxi Formation, South China

Yichen Liu [a,b,c], Benzhong Xian [a,b,c,*], Qianran Wu [a,b,c], Zhiyong Lu [d], Haocheng Shi [a,b,c], Mingjin Wu [a,b,c], Zhiyun Yu [a,b,c], Lin Zhao [a,b,c], Junyang Geng [a,b,c], Haiying Chen [a,b,c]

[a] Hainan Institute of China University of Petroleum (Beijing), Sanya 572025, China
[b] State Key Laboratory of Petroleum Resources and Prospecting, China University of Petroleum (Beijing), Beijing 102249, China
[c] College of Geosciences, China University of Petroleum (Beijing), Beijing 102249, China
[d] Sinopec Jianghan Oilfield Branch Company, Qianjiang, Hubei 433124, China

ARTICLE INFO

Keywords:
Relative sea-level change
Cyclostratigraphy
Bottom-current erosion
Evolutive spectral analysis
Sequence stratigraphy

ABSTRACT

Fine-grained successions, traditionally interpreted as continuous archives, contain cryptic hiatuses that are critical for evaluating stratigraphic completeness and paleoenvironmental evolution but remain difficult to resolve, especially in deep-water black shales. This study identifies six hiatuses (H1–H6) in the Lower Silurian Longmaxi Formation through integrated sedimentology, cyclostratigraphy, geochemistry, and Evolutive Spectral Analysis (ESA). A 405 kyr eccentricity-tuned astronomical timescale combined with sedimentary noise modeling yields a third-order relative sea-level (RSL) curve, demonstrating controls from both glacio-eustasy and the Kwangsian Orogeny. Our results demonstrate that hiatuses H1–H4 and H6 align with RSL falls, as evidenced by erosion, oxidation, and enhanced bottom-current/gravity-flow activity under cooler climates. Conversely, H5 formed during a warmer highstand, characterized by intense bioturbation and sediment starvation, indicating a non-depositional hiatus. We propose a classification scheme linking ESA spectral features (spectral bifurcation/shifts) with sedimentary attributes, defining seven hiatus types. The Results highlight sea-level fall-driven bottom-current and gravity-flow erosion as the primary hiatus-forming mechanism in deep-water settings. Third-order RSL fluctuations generate major erosional and non-depositional hiatuses (million-year scale), whereas higher-frequency fluctuations induce more subtle and cryptic hiatuses. These surfaces serve as key sequence boundaries, refining sequence stratigraphic frameworks in fine-grained systems. The integrated approach provides a robust methodology for recognizing hiatuses and advances understanding of sedimentary dynamics in deep-water successions.

1. Introduction

Unconformities represent significant temporal gaps in the geological record, traditionally interpreted as products of subaerial exposure or shallow-water erosion (Wheeler, 1964; Catuneanu, 2022). Conventionally, fine-grained successions (defined as containing at least 50 % particles <62.5 μm) have been attributed to quiescent, continuous suspension settling in low-energy environments (Trabucho-Alexandre, 2015; Atar et al., 2019; Boulesteix et al., 2019). Consequently, such successions were long assumed to be stable, devoid of unconformities, and to constitute high-fidelity archives of geological history, encompassing both terrestrial (e.g., deep lacustrine) and marine deep-water settings, e.g., shelf-slope systems, and abyssal plains (Potter et al., 2005; Macquaker et al., 2007; Bhattacharya and MacEachern, 2009; Schieber and Southard, 2009; Bohacs et al., 2014; Lazar et al., 2015b; Paz et al., 2022; Cao et al., 2024).

However, recent studies challenge this paradigm, revealing that stratigraphic discontinuities—including intermittent sedimentation breaks and discontinuous depositional events—occur within these seemingly stable successions in subaqueous environment, regardless of depositional settings (shallow- or deep-water; Schieber, 1994; Hickey and Henk, 2007; Loucks and Ruppel, 2007; Macquaker and Bohacs, 2008; Schieber and Southard, 2009; Wilson and Schieber, 2015; Kemp et al., 2018; Boulesteix et al., 2019; DeReuil and Birgenheier, 2019; Stow

* Corresponding author at: Hainan Institute of China University of Petroleum (Beijing), Sanya 572025, China.
E-mail address: xianbzh@cup.edu.cn (B. Xian).

https://doi.org/10.1016/j.coal.2025.104869
Received 11 July 2025; Received in revised form 26 August 2025; Accepted 28 August 2025
Available online 2 September 2025

and Smillie, 2020; Plantz et al., 2024; Cao et al., 2024). Critically, investigations stemming from the Deep Sea Drilling Project (DSDP) and Integrated Ocean Drilling Program (IODP) demonstrate widespread marine hiatuses, indicating that regions previously assumed to represent consistent deposition are frequently interrupted by high-intensity erosional events or prolonged periods of non-deposition (Macquaker and Bohacs, 2008; Dutkiewicz and Müller, 2022). Further research on turbidite and contourite depositional systems has revealed that such stratigraphic discontinuities in marine settings may be attributed to various processes, including sedimentation starvation (Nordsvan et al., 2025), changes in seawater corrosiveness (Barron and Keller, 1982), seafloor winnowing and ventilation (März et al., 2011; Hansen and Passchier, 2017), diagenetic overprinting (Greene et al., 2020), erosive hydrodynamics (e.g., bottom currents, turbidity flows, internal waves, storm-induced waves, and mesoscale eddies; Ankindinova et al., 2020; Dutkiewicz and Müller, 2022; Beelen and Wood, 2023), and mass transport processes (Ineson et al., 2022; Nugraha et al., 2022).

These stratigraphic breaks in fine-grained successions, often termed 'hiatuses' or 'hiatal surfaces' (Christ et al., 2012; Miall, 2016; Gani, 2017; Paola et al., 2018), can now be identified through various approaches: (i) sediment physical properties changes (e.g., lithology, color reflectance, and particle size; Elad et al., 2022; Tagliaro et al., 2022; Moshe et al., 2024); (ii) geophysical well-logging anomalies (Salazar et al., 2023); (iii) microfossil community disruptions (e.g., planktonic foraminifera, diatoms, and radiolarians; Johnson, 1974; Berggren, 1978); (iv) abrupt geochemical shifts (Ivanova et al., 2020; French et al., 2024); (v) indicators of non-deposition (e.g., ferromanganese nodules, phosphates, microbial crusts, intense bioturbation, and mineralized hardgrounds; Kennett and Watkins, 1975; Álvaro and Clausen, 2006; Föllmi, 2016); and (vi) ichnological, magnetostratigraphic, or cyclostratigraphic analyses (Barnett and Wright, 2008; Hilgen et al., 2015; Farouk et al., 2022; Rodríguez-Tovar, 2022; Nie et al., 2023).

Despite being well-documented in the literature, hiatuses within fine-grained, deep-water successions remain significantly less explored and understood compared to their more conspicuous counterparts on shorefaces, tidal flats, and shallow carbonate platforms (Hillgaertner, 1998; Sattler et al., 2005; Christ et al., 2012; Christ et al., 2015; Strasser, 2015; Brady and Bowie, 2017; Wroblewski and Morris, 2023). Their subtle, cryptic nature poses major challenges to identifiying and constraining the genesis of these hiatuses (Sommerfield, 2006; Miall, 2016). Furthermore, robust detection typically requires integrated, multi-proxy approaches (e.g., sedimentology, diagenesis, ichnology, and micropaleontology) that are time-consuming and labor-intensive, while concise, widely applicable methods are still lacking widespread adoption (Meyers and Sageman, 2004; Smith et al., 2015). Moreover, the relative roles of autogenic (e.g., event deposits) versus allogenic (e.g., eustasy, tectonism, and climate change) controls on hiatus formation remain debated (Tomer et al., 2011; Miall, 2015; Hajek and Straub, 2017; Braithwaite, 2020; Burgess and Duller, 2024).

The Lower Silurian Longmaxi Formation of the Yangtze Platform, South China, provides an exceptional opportunity to address these knowledge gaps regarding hiatuses in fine-grained depositional systems. This formation comprises extensive graptolitic black shales across the Yangtze platform, and recent sedimentological and petrographic studies have revealed compelling evidence for active bottom currents and gravity flows within these deposits (Wang et al., 2019b; Yang et al., 2021; Qiu et al., 2022; Lu et al., 2023), directly implicating dynamic processes capable of generating hiatuses in subaqueous settings. This study focuses specifically on the first member of the Longmaxi Formation (Long-1 Member) in the Sichuan Basin. The primary objectives of this study were to: (i) identify and document the characteristics of hiatuses within fine-grained deposits and interpret their genesis; (ii) elucidate the relationship between hiatuses and transgressive-regressive third-order cycles minima driven by cold climatic conditions and tectonic uplift; (iii) establish a multi-factor genetic classification scheme for hiatuses, based on evolutive spectral analysis, to facilitate identification and determination of their formation mechanisms; and (iv) examine the hierarchical nature of hiatuses, recognizing that high-rank hiatuses are associated with significant non-depositional or erosional events occurring on million-year (third-order) timescale. Consequently, hiatuses may serve as sequence boundaries within fine-grained successions, and this study aims to enhance the current understanding of fine-grained sequence stratigraphy.

2. Geological setting

2.1. Regional geology

The Sichuan Basin, situated in southwestern China, is a typical superimposed basin within the South China Plate that has undergone multiple tectonic episodes (Liu et al., 2021). The study area, Fuling, is located in the southeastern part of the Sichuan Basin. The well location map, tectonic development patterns, and stratigraphic column for this area are presented in Fig. 1. During the Early Silurian, the South China Plate was positioned along the northern margin of Gondwana at a paleolatitude near the equator (Fig. 2A; Liu et al., 2017). This region comprises two major blocks: the Yangtze Platform and Cathaysia Land (Chen et al., 2010). Extensive graptolitic black shales of the Longmaxi Formation was deposited across the Yangtze Platform, primarily driven by the melting of the Gondwana ice sheet and the subsequent transgression (Fig. 2B; Lu et al., 2023; Nie et al., 2024).

Coinciding with this period, the Yangtze Platform and Cathaysia Land collided and amalgamated, generating significant tectonic activity (Nie et al., 2024). This convergence established a compressive tectonic regime in the Sichuan Basin, leading to a platform-slope-basin geomorphological configuration within an epicontinental shelf environment (Fig. 2B; Chen et al., 2014; Yang et al., 2020; Wang et al., 2023a, 2023b). The collision also initiated the Kwangsian Orogeny (460–400 Ma; Xu et al., 2016), characterized by regional folding, ductile deformation, and vertical tectonic uplift and subsidence (Yang et al., 2019). These processes produced a paleogeomorphology defined by paleouplifts, submarine highs, and depressions, with estimated water depths of approximately 200 m (Fig. 2B; Liang et al., 2016; Li et al., 2017a; Jin et al., 2021; Nie et al., 2024). This paleogeomorphology exerted strong control on the sedimentation patterns and depositional architecture of the Longmaxi Formation, contributing to its complex present-day stratigraphic framework. Furthermore, the migration of the depocenter closer to sediment source areas promoted frequent gravity-driven processes, including turbidity currents and slumping (e.g., Liu et al., 2017; Lu et al., 2020; Shen et al., 2021; Lu et al., 2023). Chen et al. (2017, 2018) revealed that the Yangtze and Yichang Uplift resulted in a stage-progressive distribution pattern within the Longmaxi Formation, accompanied by stratigraphic hiatuses during the Rhuddanian–Aeronian periods.

2.2. Chronostratigraphy and biostratigraphy framework

The Longmaxi Formation is subdivided into three members: Long-1, Long-2, and Long-3 Members. The Long-1 Member encompasses seven graptolite biozones (*LM2-LM8*; Fig. 2C; Chen et al., 2017). The basal *Akidograptus ascensus* Biozone *(LM2)* marks the onset of the Rhuddanian stage (443.07 Ma), while the uppermost *Stimulograptus sedgwickii* Biozone *(LM8)* occurs near the termination of the Aeronian stage (438.59 Ma), representing a total duration of 4.48 Myr for the Long-1 Member. The Rhuddanian-Aeronian boundary, which coincides with the base of the *Demirastrites triangulatus* Biozone (*LM6*), is demarcated by regionally extensive volcanic ash layers (440.77 Ma; Shen et al., 2021).

Previous studies have proposed the overlying turbidite deposits as a potential termination marker for the Long-1 Member. However, the multi-stage nature of such event deposits renders turbidites unreliable for establishing precise isochronous constraints. Consequently, the development of novel, robust methodologies is essential to accurately

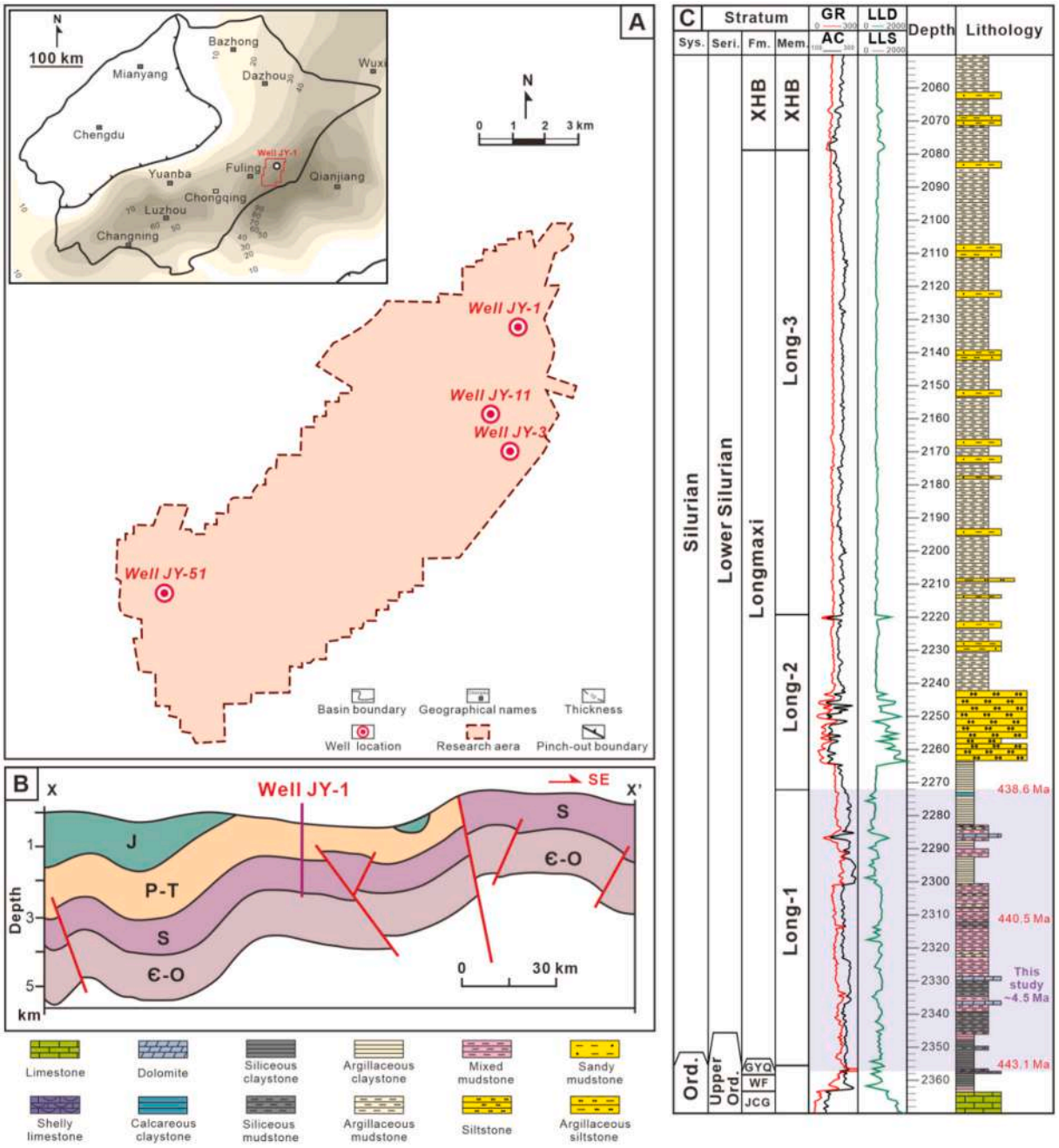

Fig. 1. Geological setting of the study area. (A) Location map of study wells. Inset map (upper left) shows thickness distribution of the Long-1 Member within the Sichuan Basin. (B) Stratigraphic development and tectonic framework profile (oriented southeastward across Well JY-1 through the study area). (C) Composite stratigraphic column spanning the Upper Ordovician Wufeng Formation to the Lower Silurian Longmaxi Formation. Abbreviations: Sys. - System; Seri. - Series; Fm. - Formation; Mem. - Member; Sub. - Submember; Ord. - Ordovician; Upper. – Upper Ordovician; XHB - Xiaoheba Formation; GYQ – Guanyinqiao Bed; WF - Wufeng Formation; JCG - Jiancaogou Formation; XHB - Xiaoheba Formation.

define the upper boundary of the Long-1 Member.

During the Early Silurian, several globally recognized positive carbon-isotope excursions provide potential chronostratigraphic markers. The Late Aeronian Event, temporally associated with the extinction of the *Sedgwickii* graptolite Biozone (*LM8*; see Fig. 2C), is characterized by a pronounced global positive $\delta^{13}C_{org}$ excursion. This isotopic event correlates with a glacial maximum and a significant eustatic sea-level fall (Melchin and Holmden, 2006; Loydell, 2007; Johnson, 2010; Munnecke et al., 2010; Storch and Frȓda, 2012; Trotter et al., 2016). Therefore, in this study, we utilized the positive $\delta^{13}C_{org}$ excursion identified in Well JY-51 as the primary criterion for defining the upper boundary of the Long-1 Member (Fig. 3).

3. Materials and methods

3.1. Logging and samples

In this study, we used geological borehole datasets from three Sinopec wells drilled into the Wufeng-Longmaxi Formations within the Fuling area: Well JY-3 (total depth: 2499 m), Well JY-11 (total depth: 2406 m), and Well JY-51 (total depth: 3178 m). Detailed geological investigations were conducted on these wells. Continuous core samples were obtained from Wells JY-11 (depth interval: 2252–2365.18 m) and JY-51 (depth interval: 3027.55–3148.53 m), whereas Well JY-3 lacked core coverage.

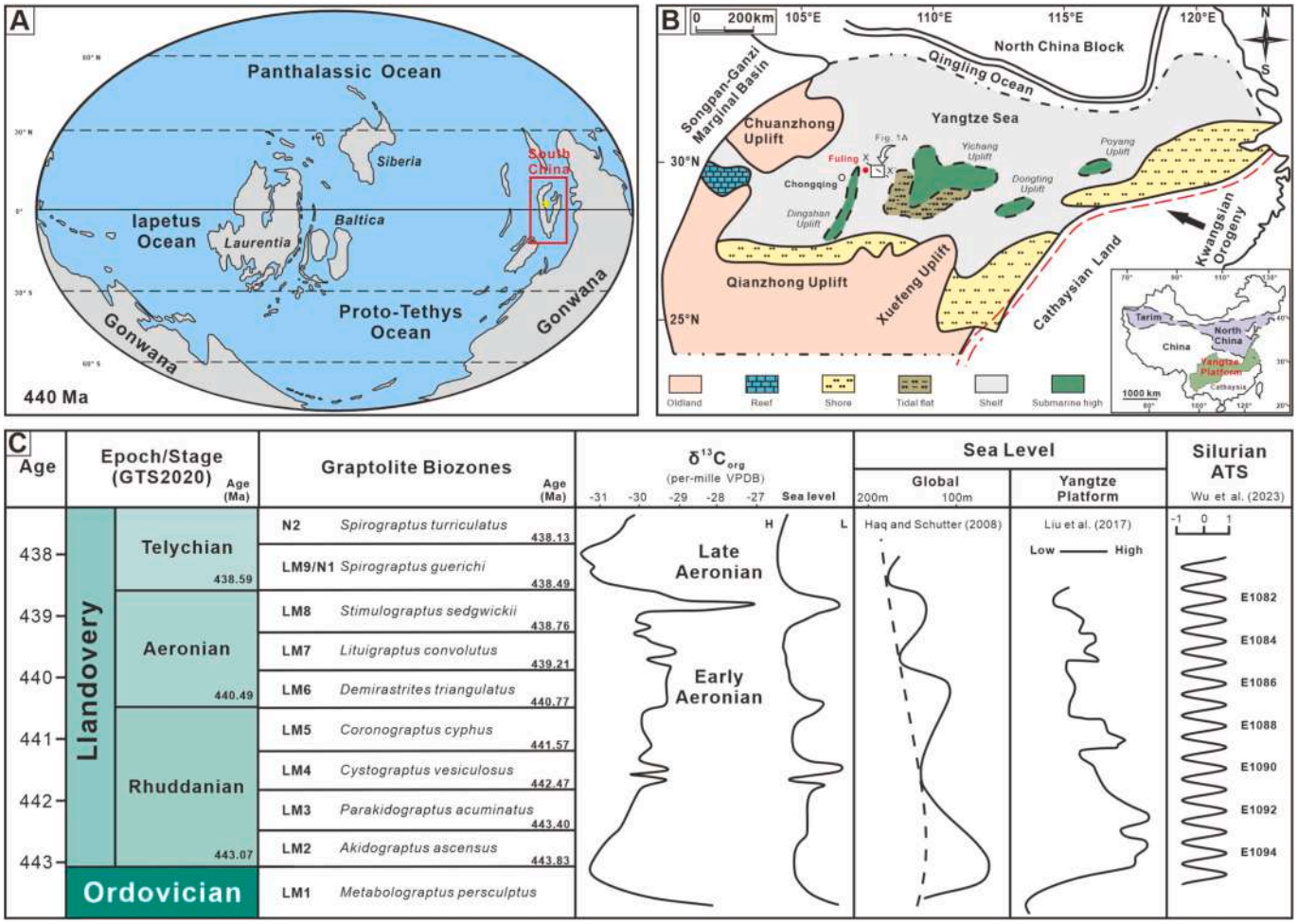

Fig. 2. Intergrated stratigraphic and paleogeographic framework of the Yangtze Platform during the Early Silurian. (A) Global paleogeographic reconstruction for 440 Ma (source: https://deeptimemaps.com). (B) Paleogeographic maps of the Yangtze Platform during Early Silurian, modified from Xu et al. (2004) and Ou et al. (2018). (C) Overview of the timescale during the Early Silurian, showing the following aspects: geological timescale (from Melchin et al., 2020); graptolite biozones (from Chen et al., 2017); major global positive carbon-isotope excursion events during the Rhuddanian and Aeronian periods (from Melchin and Holmden, 2006); global (from Haq and Schutter, 2008) and Yangtze Platform (from Liu et al., 2017) sea-level curves; and astronomical timescale (from Wu et al., 2023).

The analyzed datasets comprised core data, geophysical well-log data, and geochemical data. Core data (including core samples and thin sections) were utilized to characterize fine-grained lithologies, textures, sedimentary structures, and the nature of stratigraphic hiatuses. Geophysical well-log data encompassed conventional logs (e.g., gamma ray, resistivity, acoustic) sampled at 0.125 m intervals, high-resolution gamma-ray (HGR) logs with a 0.05 m sampling resolution, and spectral gamma-ray measurements of thorium (Th), uranium (U), and potassium (K). These logs were employed for cyclostratigraphic analysis, identification of sedimentary hiatuses, and interpretation of depositional environments; elemental ratios derived from spectral gamma-ray logs (e.g., Th/U) were calculated to constrain depositional redox conditions. Geochemical data—including major and trace elements, total organic carbon (TOC), total sulfur (TS), and organic carbon isotopes ($\delta^{13}C_{org}$)—were used for stratigraphic correlation and to reconstruct terrigenous input, paleoclimate, and redox conditions.

3.2. Analytical methods

3.2.1. Time series analysis

Cyclostratigraphy provides a high-resolution chronometer for constructing precise isochronous stratigraphic frameworks (Meyers et al., 2001; Zeebe and Kocken, 2024), thereby offering a foundation for the spatiotemporal correlation of stratigraphic hiatuses. For cyclostratigraphic time series analysis, the software Acycle v2.7 was employed (Li et al., 2019).

Natural gamma-ray (GR) logging reflects the enrichment of thorium (Th), uranium (U), and potassium (K) in sediments. These elements are primarily concentrated in clay minerals and organic matter due to their strong affinity for these radioactive elements (Ruffell and Worden, 2000; Schnyder et al., 2006; Li et al., 2016). The relative abundance of radioactive-elements-enriched clay and organic matter typically serves as a robust indicator of paleoclimate conditions (e.g., precipitation and continental weathering intensity). Under warm and humid climates, intensified chemical weathering or increased runoff promotes the formation of clay minerals and organic matter, resulting in the enrichment of radioactive elements and elevated GR values (Zhang et al., 2022). Furthermore, in deep-water settings, mudstones generally exhibit GR values between 120 and 180 API, whereas shales show significantly higher values, often exceeding 180 API. In contrast, siltstones and sandstones typically have GR values below 120 API (Cao et al., 2024). This correlation between GR and lithology suggests that high-frequency variations in natural gamma-ray responses can effectively reflect changes in depositional environments (e.g., sea-level fluctuations). The GR log is thus exceptionally responsive to changes in paleoclimate and paleoenvironment, establishing it as a valuable proxy for reconstructing astronomically forced cycles of climate and sea-level change.

To identify periodic and quasi-periodic signals within the

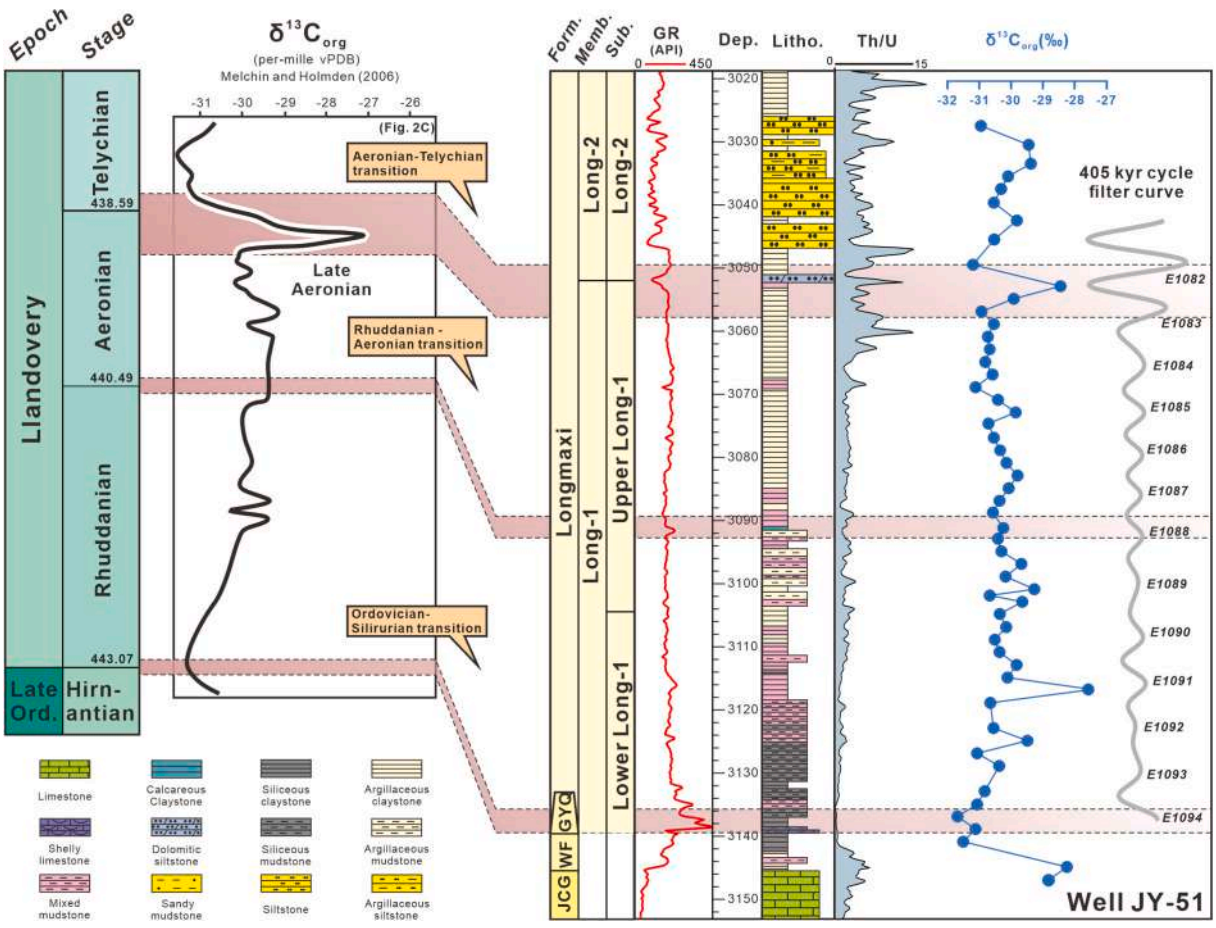

Fig. 3. Determination of the top boundary of the Long-1 Member. The boundary corresponds to the Late Aeronian Event and is marked by a prominent positive carbon isotope exursion ($\delta^{13}C_{org}$) at 3052 m depth in Well JY-51 (highlighted).

stratigraphic succession against background noise, a 2π Multi-taper Method (MTM) spectral analysis was performed on high-resolution gamma-ray logging data (HGR; 0.05 m sampling rate) (Thomson, 1982; Thomson, 1990). A robust red-noise test was applied to validate the detected astronomical signals (Mann and Lees, 1996; von der Heydt et al., 2021). Previous studies have suggested that during the Early Silurian, the long eccentricity cycle (E) exhibited a dominant period of 405 kyr, while short eccentricity cycles (e) displayed stable periods of ~125 and ~ 95 kyr (Fang et al., 2019; Jin et al., 2020; Wu et al., 2023). In contrast, obliquity and precession cycles displayed greater temporal variability during this period (Berger and Loutre, 1994; Laskar, 2008; Zeeden et al., 2023). According to the astronomical solution proposed by Waltham (2015), which incorporates tidal dissipation effects, the obliquity cycle in the Early Silurian (~ 441 Ma) is estimated at 33.4 ± 3.8 kyr. The precession cycle comprised multiple components with periods of 20.9 ± 1.5 kyr, 19.9 ± 1.3 kyr, 17.1 ± 1.0 kyr, and 17.2 ± 1.0 kyr. These target orbital periodicities served as fundamental parameters for subsequent time series analysis.

Correlation coefficient (COCO) and evolutionary correlation coefficient (eCOCO) analysis were conducted to estimate optimal sedimentation rates for the study succession (Li et al., 2018b). In COCO analysis, the most probable sedimentation rate corresponds to the peak correlation coefficient and the lowest null hypothesis test value. eCOCO analysis, employing a sliding window approach derived from COCO, reflects the vertical evolution of the optimal sedimentation rate within the stratigraphic succession (Li et al., 2018b).

Following the identification of reliable Milankovitch cycle bands through spectral analysis, the relatively stable 405 kyr long eccentricity cycle provided the basis for orbital tuning (Laskar, 2008; Wang et al., 2024). A Gaussian bandpass filter was applied to extract the 405 kyr cycle signal from the detrended GR data. Subsequently, the GR record was tuned to the stable 405 kyr eccentricity cycle.

Based on the tuned natural gamma-ray (GR) logging data, sedimentary noise modeling (both DYNOT and ρ_1 models) within Acycle v2.7 was applied to reconstruct past million-year-scale (third-order cycles) relative sea-level fluctuations in a marginal marine environment, following the approach of Li et al. (2018a). This method is founded on the concept that cyclostratigraphic proxy series contain both orbital signals and non-orbital sedimentary noise, the latter of which is influenced by depositional processes sensitive to water-depth variations (e.g., storms, tides, bioturbation, and events deposition).

The modeling operates under the hypothesis that, in a stable sedimentary environment with relatively consistent terrigenous input and basin configuration, sedimentary noise is inversely correlated with relative sea level: enhanced noise levels are interpreted to reflect shallower water depths (e.g., during lowstands), whereas reduced noise corresponds to deeper water conditions (e.g., during highstands). This relationship has been validated in several Phanerozoic successions as a proxy for relative sea-level change (Huang et al., 2021; Wang et al., 2023a, 2023b; Wei et al., 2023; Zhang et al., 2023a, 2023b).

3.2.2. *Detection of hiatus*

Depositional hiatuses represent critical archives of sedimentation history, particularly when astronomical orbital forcing is clearly expressed within the stratigraphic column and a high-resolution astronomical timescale is established. Previous studies have demonstrated

that hiatuses can introduce distortions in the frequency domain of cyclostratigraphic signals (Meyers et al., 2001; Weedon, 2003; Meyers and Sageman, 2004). Meyers et al. (2001;2004) suggested a robust methodology for detecting hiatuses within rhythmically-bedded strata using evolutive spectral analysis (ESA). This technique, implemented by applying a sliding window to spectral analysis, facilitates the quantitative identification of depositional hiatuses within the frequency domain. ESA tracks temporal variations in dominant frequencies preserved in stratigraphic column by identifying abrupt shifts or gradual drifts in spectral power, thereby revealing depositional hiatuses and erosional events. Consequently, this study employs ESA to dynamically identify stratigraphic discontinuities within the examined section (Long-1 Member). Critically, hiatuses were identified based on diagnostic features in the evolutive spectral analysis, including bifurcated spectral peaks and abrupt or gradual shifts in spectral power, which signify sudden changes in sedimentation rate, erosional events, and depositional gaps.

3.2.3. Geochemical and mineralogical analyses

To diagnose the genetic mechanisms of sedimentary hiatuses, a suite of geochemical and mineralogical analyses was performed on core samples from Wells JY-11 and JY-51. Detailed analytical procedures, instrumentation, and calculation methods, alone with a summary of all proxies employed and their environmental interpretations, are provided in Supplementary Materials (Text S1 and Table S1, respectively).

4. Results

4.1. Lithological classification and characteristics of shale

The lithology of Long-1 Member was classified based on the grain size of fine-grained rocks identified through thin-section analysis and mineral composition (Fig. 4A, Aplin and Macquaker, 2011; Lazar et al., 2015a). For grain size classification, a ternary diagram was constructed using sand, coarse mud, and fine mud as end members. Within this ternary space, "fine-grained sedimentary rocks" was defined as containing ≥50 % fine-grained particles (<62.5 μm). Under this broad category, fine-grained sedimentary rocks were further subdivided into claystone, mudstone, and siltstone based on whether specific size-range fractions exceeded two-third of the total composition, serving as the basis for rock nomenclature.

Mineral composition data were obtained through X-ray diffraction (XRD) analysis, with total quartz, carbonate (e.g., calcite, dolomite), and argillaceous (e.g., illite, smecite) components serving as the primary end-members (Fig. 4A). The fine-grained sedimentary rocks (e.g., claystone, mudstone, and siltstone) were classified according to the dominant component(s) exceeding 50 %. If no single component exceeded 50 %, the fine-grained sedimentary rocks were classified as "mixed". Based on the above classification framework, the fine-grained sedimentary rocks in the Long-1 Member primarily consist of siliceous, argillaceous, and mixed claystone/mudstone, with minor occurrences of calcareous claystone, argillaceous siltstone, and calcareous siltstone (Fig. 4).

Based on vertical variations in lithological characteristics, the Long-1 Member can be further subdivided into upper and lower sections. The lower section is dominated by black, organic-rich siliceous claystone/

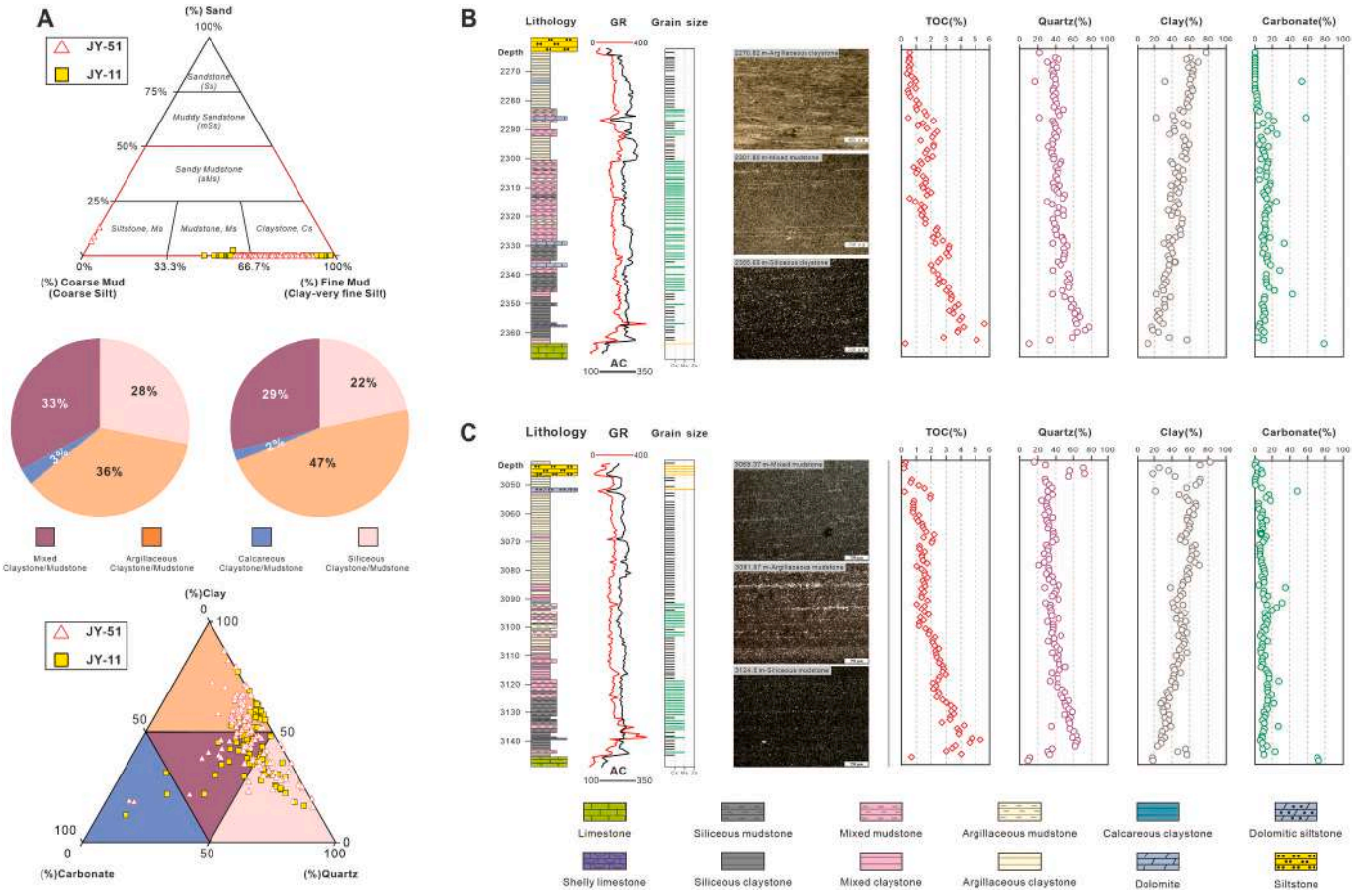

Fig. 4. Lithological characterization of the Long-1 Member (A) Lithological classification framework and percentage composition of fine-grained lithofacies in Wells JY-11 and JY-51. (B, C) Intergrated lithological, geophysical, total organic carbon (TOC) and mineralogical content for Long-1 Member in Wells JY-11 and JY-51.

mudstone and mixed claystone, and mudstone, while the upper section predominantly comprises gray-colored argillaceous claystone and mudstone with low organic carbon content. In Well JY-11, grain size analysis reveals that both the base and top of the Long-1 Member are predominantly composed of claystone, while the middle section shows coarser-grained sediments. Mineral composition analysis demonstrates that the Long-1 Member is characterized by an overall low carbonate mineral content (<3 %), with quartz and argillaceous minerals dominating the composition (Fig. 4B). Vertically, quartz shows a gradual decreasing trend, while argillaceous minerals display an opposite increasing trend. The total organic carbon (TOC) content exhibits an overall decreasing trend upward through the stratigraphic column (Fig. 4B). In Well JY-51, located in the southern region of the study area, the vertical variations in particle grain size, mineral composition, and total organic carbon exhibit similar pattern to those observed in Well JY-11, but with significantly enhanced argillaceous mineral content. The lower section of Long-1 Member in Well JY-51 contains fine-grained sedimentary rocks with lower quartz content compared to that in Well JY-11, while the upper section exhibits an increase in argillaceous content (Fig. 4C).

4.2. Time series analysis

4.2.1. Spectral analysis in the stratigraphic domain

To extract astronomical signals independent of long-term trends, this study employed a 30 m window length for detrending using the Locally Weighted Regression (LOWESS) method. The Multi-taper Method (MTM) spectral analysis of the detrended gamma-ray (GR) data from Wells JY-3, JY-11, and JY-51 revealed multiple significant peaks exceeding the 90 % confidence level (CL) (Figs. 5A-5C). In Well JY-3, peaks above the 90 % CL were detected at 14.7–23.1 m, 8.2–11.8 m, 5.7–6.1 m, 4.4–4.7 m, 2.5 m, 2.2–2.3 m, 1.6 m, 1.3 m, and 1.1 m (Fig. 5A). Similarly, Well JY-11 exhibited significant peaks above the 90 % CL at 17.1 m, 7.5–10.8 m, 5.5 m, 3.8 m, 1.8 m, 1.6 m, 1.5 m, 1.1 m and 1.0 m (Fig. 5B). For Well JY-51, prominent peaks exceeding the 90 % CL were observed at 17.5–27.8 m, 9.9 m, 8.0 m, 5.6–6.0 m, 3.2 m, 2.7–2.8

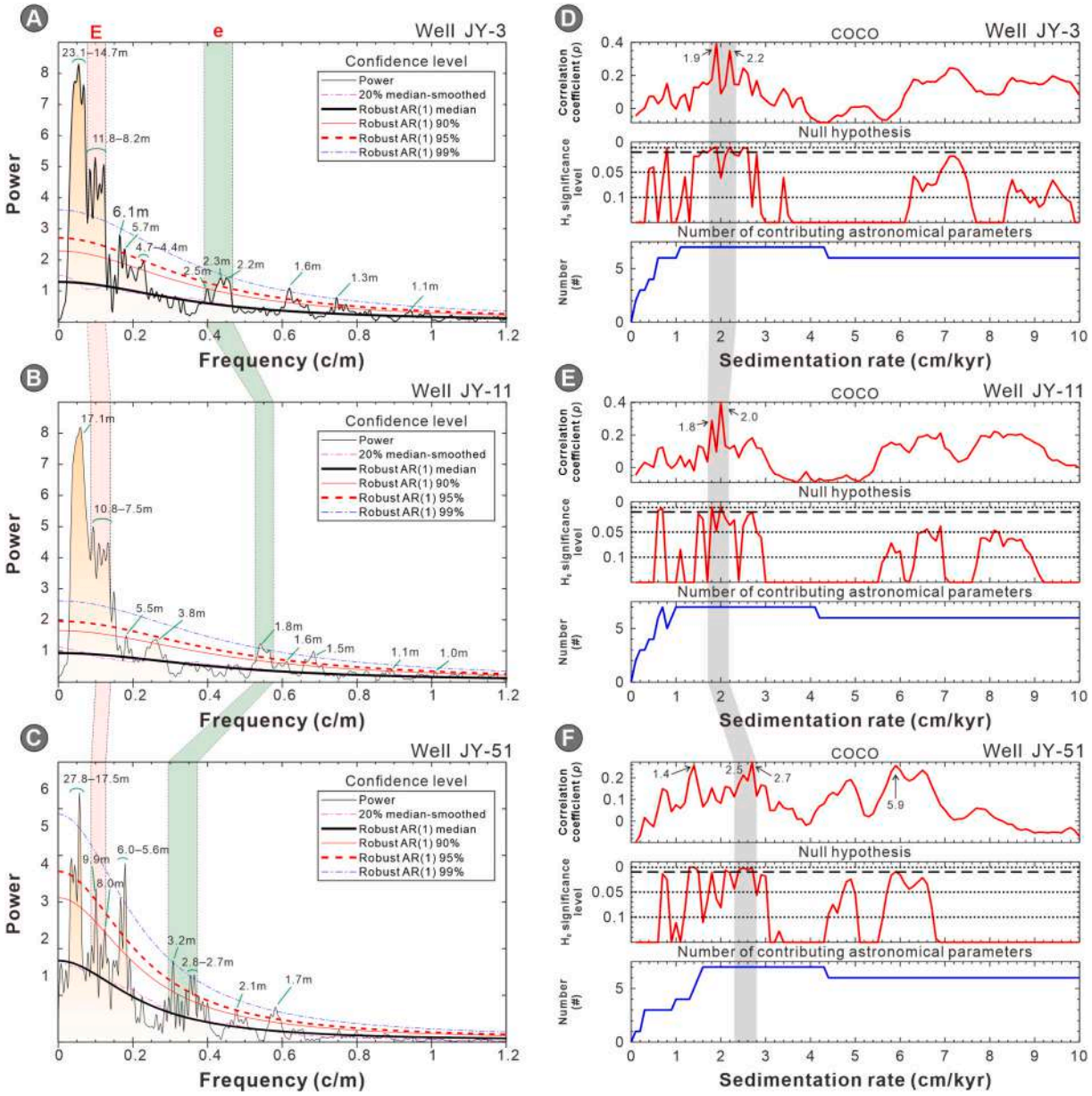

Fig. 5. Results of the 2π Multi-taper Method (MTM) spectral analysis and the 5000 Monte Carlo simulations-based correlation coefficient (COCO) analysis conducted in this study. Confidence levels (CL) for the spectral analysis were 99 %, 95 %, 90 %.

m, 2.1 m and 1.7 m (Fig. 5C).

COCO analysis indicated that the sedimentation rate of the Long-1 Member in Well JY-3 likely ranges from 1.9 to 2.2 cm/kyr, characterized by higher correlation coefficients, lower null hypothesis test values, and greater contributions from astronomical orbital parameters (Fig. 5D). Similarly, the probable sedimentation rate for Well JY-11 was estimated to be 1.8–2.0 cm/kyr (Fig. 5E). Well JY-51 exhibited complex sedimentation rate characteristic, with higher correlation coefficients and lower null hypothesis test values observed at 1.4 cm/kyr, 2.5–2.7 cm/kyr, and 5.9 cm/kyr (Fig. 5F). However, the number of contributing astronomical parameters at 1.4 cm/kyr and 5.9 cm/kyr was relatively low, suggesting that the range of 2.5–2.7 cm/kyr is the most probable optimal sedimentation rate.

The eCOCO results demonstrated that the sedimentation rate interval of 1.9–2.2 cm/kyr in Well JY-3 remained vertically stable throughout the Long-1 Member (Fig. 6A). In Well JY-11, the sedimentation rate interval of 1.8–2.0 cm/kyr similarly maintained vertical stability (Fig. 6B). For Well JY-51, the sedimentation rate remained relatively stable at 2.5–2.7 cm/kyr across the entire stratigraphic column (Fig. 6C).

Based on the inferred optimal sedimentation rate range of 1.9–2.2 cm/kyr derived from COCO and eCOCO analysis for Well JY-3, the thickness intervals of 8.2–11.8 m may correspond to a time span of 373–621 kyr. The 2.5 m cycle likely represents a duration of 114–132 kyr, and the 2.2–2.3 m intervals may correspond to 105–121 kyr. Similarly, for Well JY-11, with an optimal sedimentation rate of 1.8–2.0 cm/kyr, the 7.5–10.8 m intervals are estimated to represent 375–600 kyr, and the 1.8 m cycle may reflect 90–100 kyr. In Well JY-51, where the most probable optimal sedimentation rate is 2.5–2.7 cm/kyr, the 9.9 m cycle likely corresponds to 367–396 kyr, the 3.2 m cycle to 119–128 kyr, and the 2.7–2.8 m cycle to 100–108 kyr.

4.2.2. *Spectral analysis in the time domain and sedimentation noise modeling*

In the Paleozoic, the identification of long eccentricity astronomical cycles was considered more stable and thus served as the basis for astronomical tuning. These cycles are numbered according to the nomenclature outlined by Wu et al. (2023). The 405 kyr long eccentricity cycle filtering curve from Wells JY-3, JY-11, and JY-51 were applied for orbital tuning (Fig. 7A-7C). The floating astronomical time scale established from the tuning results indicates that the duration of the Long-1 Member is 4.45 Myr in Well JY-3 (Fig. 7A), 4.43 Myr in Well JY-11 (Fig. 7B), and 4.57 Myr in Well JY-51 (Fig. 7C). This study anchored the floating astronomical time scale to an absolute astronomical time scale using the top boundary of *LM2* as a reference (Ordovician-Silurian boundary, 443.07 Ma in GTS 2020). Spectral analysis in the time domain revealed significant cycles of 405 kyr, 243 kyr, 178 kyr, 125 kyr, 105 kyr, 77 kyr, 56 kyr, 50 kyr, 47 kyr, and 39 kyr in Well JY-3 (Fig. 7A); 405 kyr, 127 kyr, 95 kyr, 76 kyr, 68 kyr, 61 kyr, 58 kyr, 50 kyr, 42 kyr, 36 kyr, and 32 kyr in Well JY-11 (Fig. 7B); and 405 kyr, 147 kyr, and 68 kyr in Well JY-51 (Fig. 7C).

Modeling of sedimentary noise provides a robust framework for reconstructing relative sea-level variations. Taking Well JY-11 as an

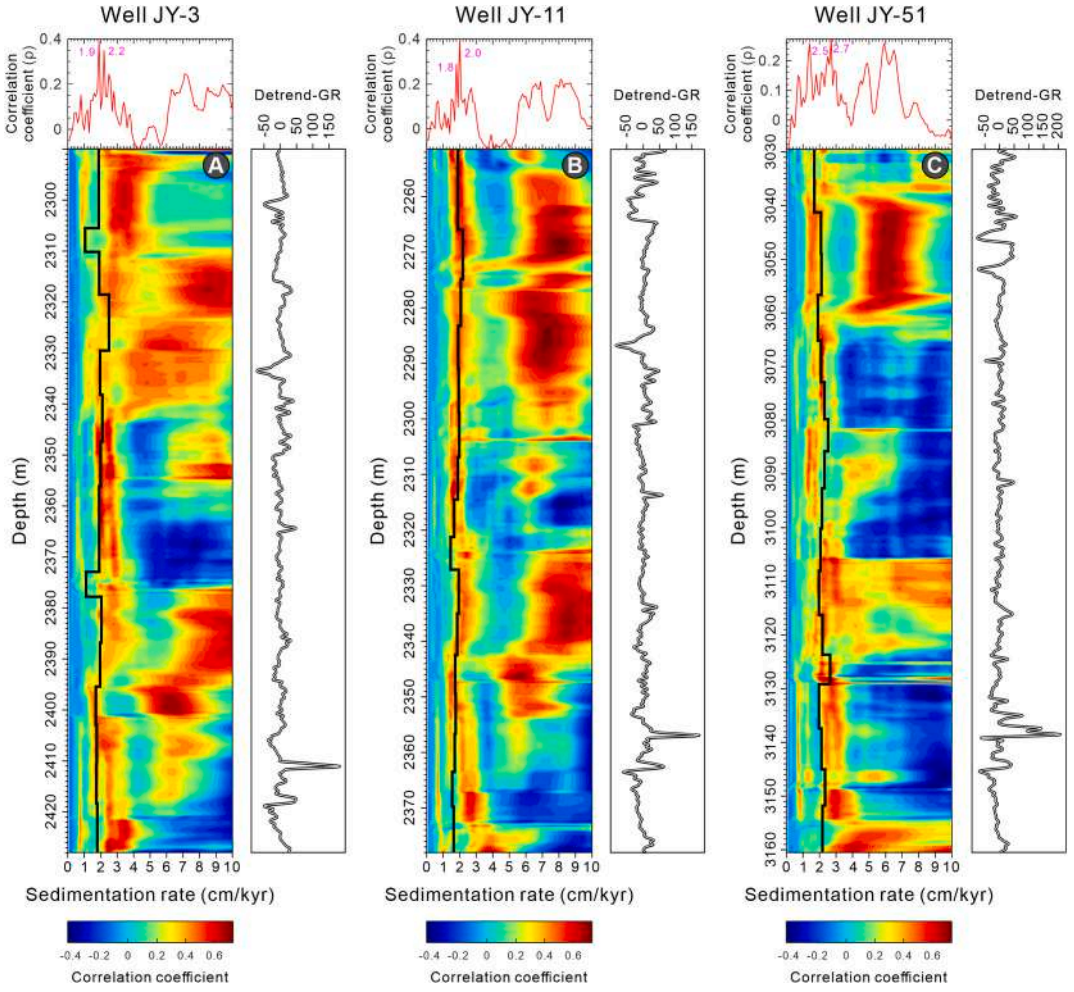

Fig. 6. Sedimentation rate analysis. (A-C) Correlation coefficient (COCO) analysis and evolutionary correlation coefficient (eCOCO) sedimentation rate maps of GR datasets in the Wells JY-3, JY-11, and JY-51. For both the COCO and eCOCO analysis, the number of Monte Carlo simulations is 5000. The sedimentation rate curves derived from interpreted 405 kyr cycles of GR data in depth domain.

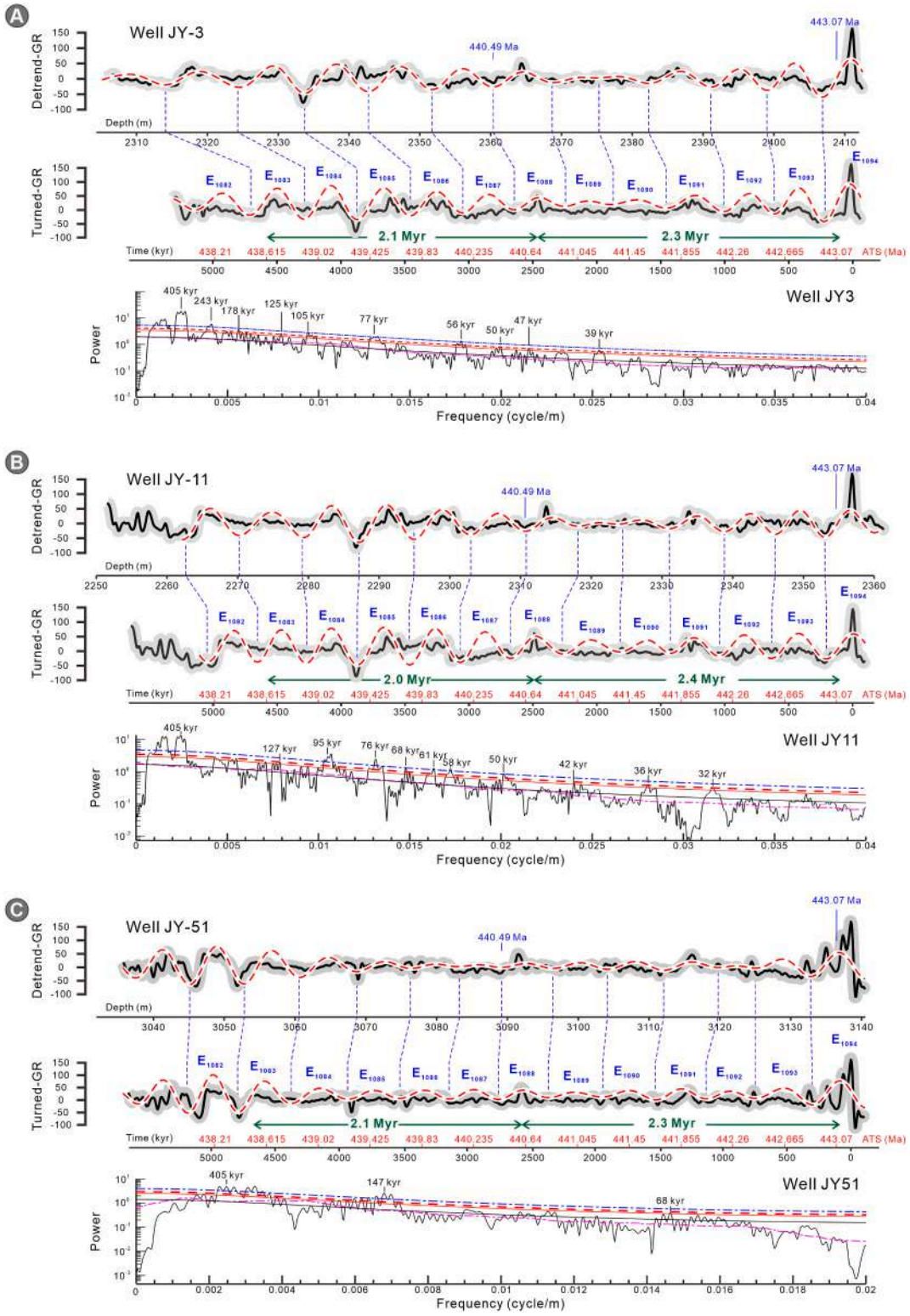

Fig. 7. Astronomical tuning and spectral analysis in time-domain for Wells JY-3, JY-11, and JY-51. The astronomical age model uses Wu et al. (2023) as a reference curve. Blue numbers denote ages from regional stratigraphic correlation and GTS2020. Red numbers denote absolute ages from the astronomical time scale constructed in this study, anchored at the top boundary of *LM2* Biozone (443.07 Ma). The Rhuddanian-Aeronian boundary position aligns well with GTS2020 (440.49 Ma). (For interpretation of the references to color in this figure legend, the reader is referred to the web version of this article.)

example, sedimentary noise curves derived from the DYNOT and ρ_1 models exhibit notable consistency. According to the established principle whereby high noise levels correspond to low sea levels and low noise levels correspond to high sea levels, we reconstructed the Early Silurian sea-level curve for the Yangtze Platform. The resulting curve reveals a recurrent "fall-rise" pattern, indicative of high-frequency, oscillatory sea-level fluctuations (Fig. 8B).

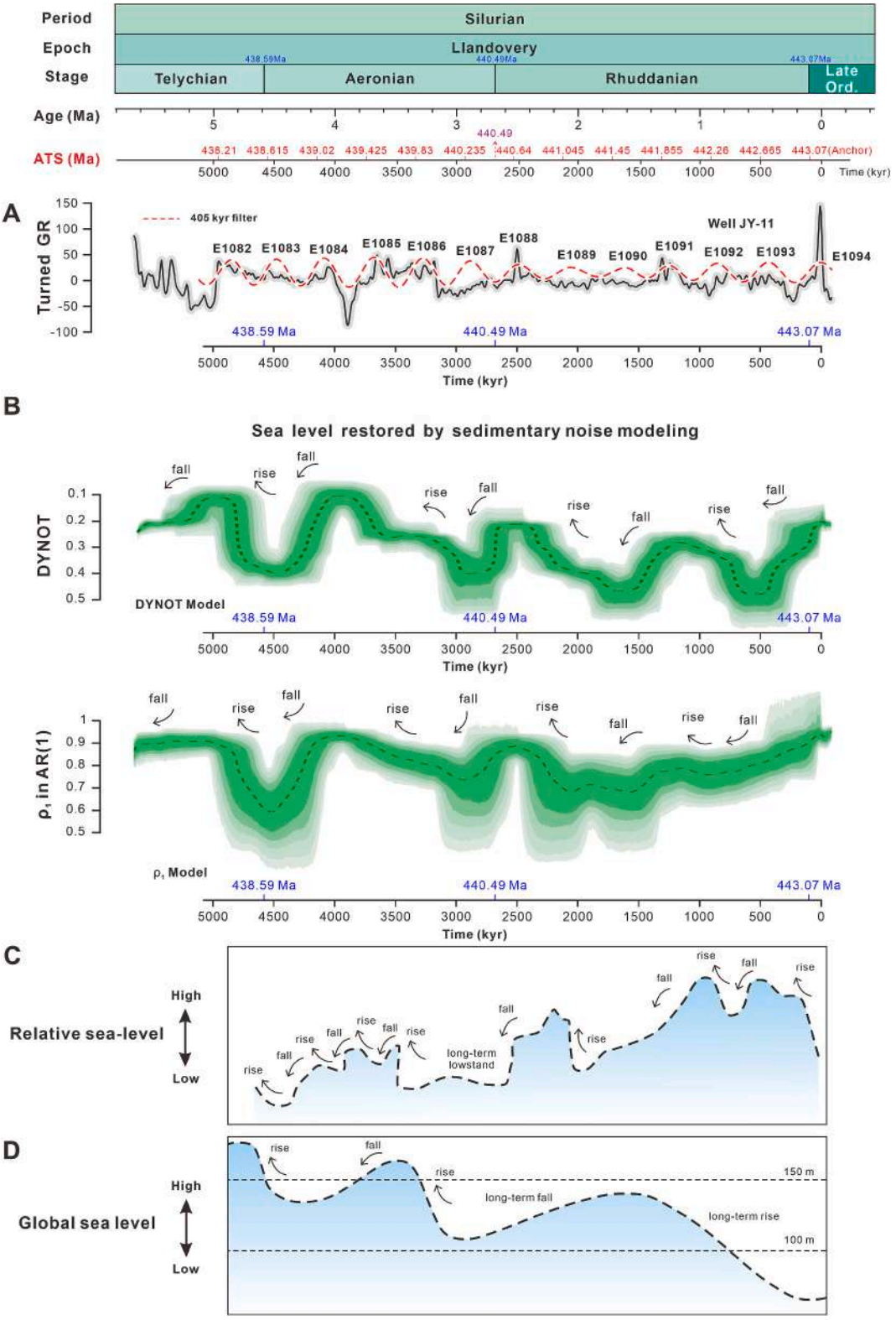

Fig. 8. Reconstructed and reference relative sea-level (RSL) for Well JY-11. (A) Astronomically tuned gamma ray (GR) log and chronostratigraphic column, with numbered 405 kyr cycles (following Wu et al., 2023). The astronomical time scale is anchored at the top boundary of *LM2* Biozone (443.07 Ma). (B) RSL fluctuation curve reconstructed using sedimentary noise models (DYNOT and ρ_1). (C, D) Reference sea-level curves for the Yangtze Platform (Liu et al., 2017) and global (Haq and Schutter, 2008) during the Early Silurian. Chronostratigraphy modified from GTS2020.

4.3. Detection and characteristics of hiatus

4.3.1. Dectection of hiatus

Hiatus identification employed Evolutive Spectral Analysis (ESA). Using a 20 m sliding window, potential hiatus characterized by bifurcations, gradual transitions, or abrupt shifts in spectral power were marked on evolutive spectral plots (Figs. 9A-9C). From the base to the top of each well, spectral bifurcations indicative of hiatuses occurred at the following depths: Well JY-3: 2420–2410 m, 2401–2396 m, 2377–2374 m, 2363–2354 m, 2346–2340 m, and 2326–2322 m (Fig. 9A); Well JY-11: 2360–2355 m, 2347–2343 m, 2326–2323 m, 2303–2315 m, 2299–2292 m, and 2277–2270 m (Fig. 9B); Well JY-51: 3142–3135 m, 3129–3121 m, 3106–3100 m m, 3093–3081 m, 3080–3072 m, and 3065–3058 m (Fig. 9C). These features preliminary indicated six potential hiatuses, designated Hiatus 1 to 6 (H1–H6). These hiatuses consistently align with minima of the 405 kyr long-eccentricity

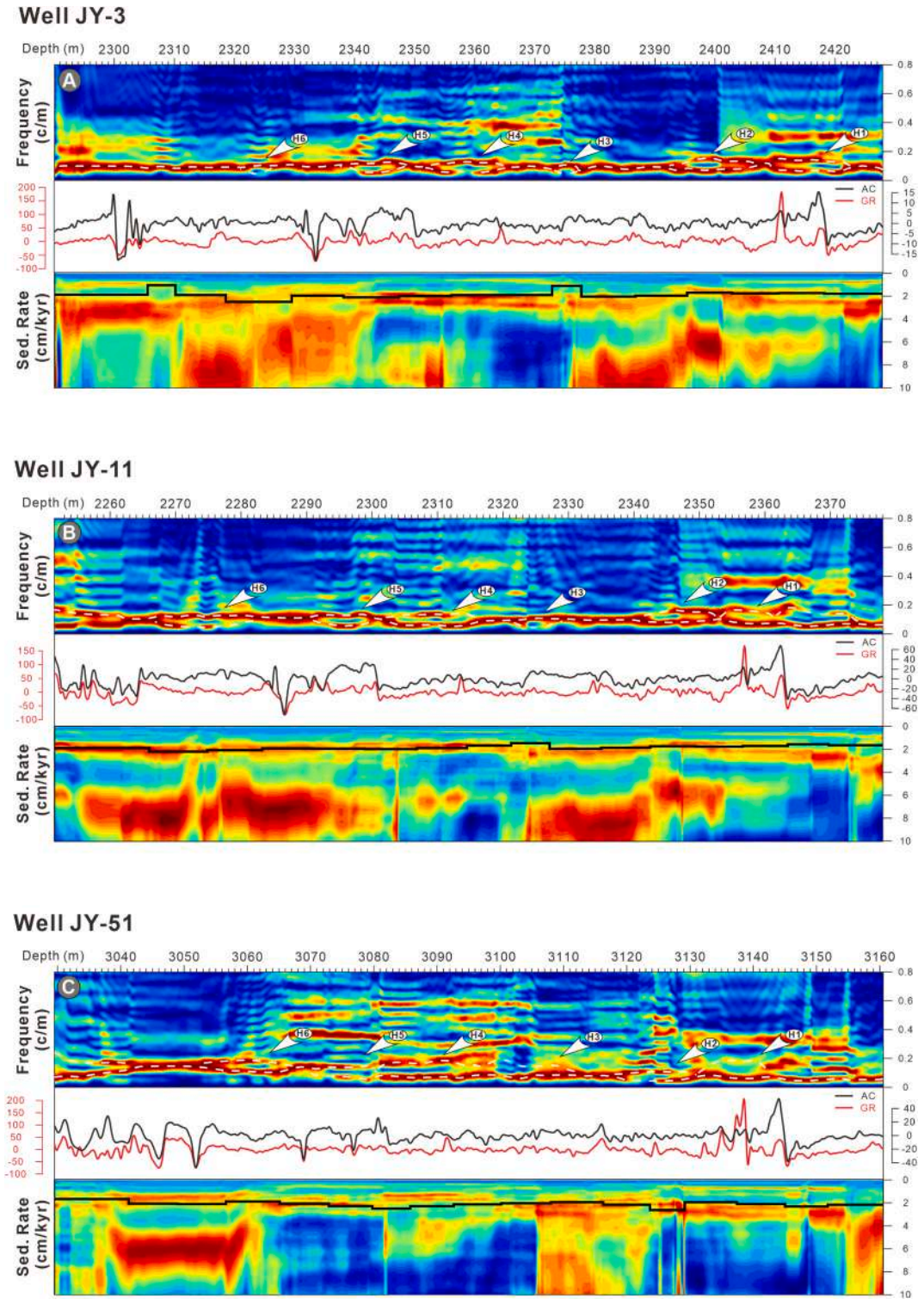

Fig. 9. Identification of stratigraphic hiatuses. Evolutive spectral analysis (ESA) and sedimentation rate variations (from eCOCO) for Wells JY-3, JY-11, and JY-51, highlighting intervals of potential hiatuses.

cycles, corresponding to the boundaries between specific cycles in the depth domain: H1 (E1094/E1095), H2 (E1092/E1093), H3 (E1089/E1090), H4 (E1087/E1088), H5 (E1085/E1086), and H6 (E1083/E1084).

4.3.2. *Petrographic characteristics of hiatus*

Integrated core characterization, grayscale analysis, and thin-section petrography validate six sedimentary hiatuses (H1–H6) within the Long-1 Member of Well JY-11. This multi-faceted approach overcomes limitations of millimeter-scale hiatus identification via evolutive spectral analysis, which relies exclusively on mathematical transformations (Fig. 10). Diagnostic characteristics distinguishing each hiatus are summarized below and detailed in Table 1.

Hiatus 1 (H1), near the *WF4-LM1* graptolite biozone transition, exhibits a sharp erosional surface overlain by higher-grayscale shelly limestone contrasting adjacent siliceous claystones (Fig. 10 Ab). Thin sections reveal weakly developed silty laminae (Fig. 10 A1-A3), with a pronounced silt influx (29–51 %) proximal to the hiatal surface. Adjacent mineralogy shows consistently high quartz (64–79 %), indicating significant clastic input, with lower clay (17–30 %) and carbonate (4–11

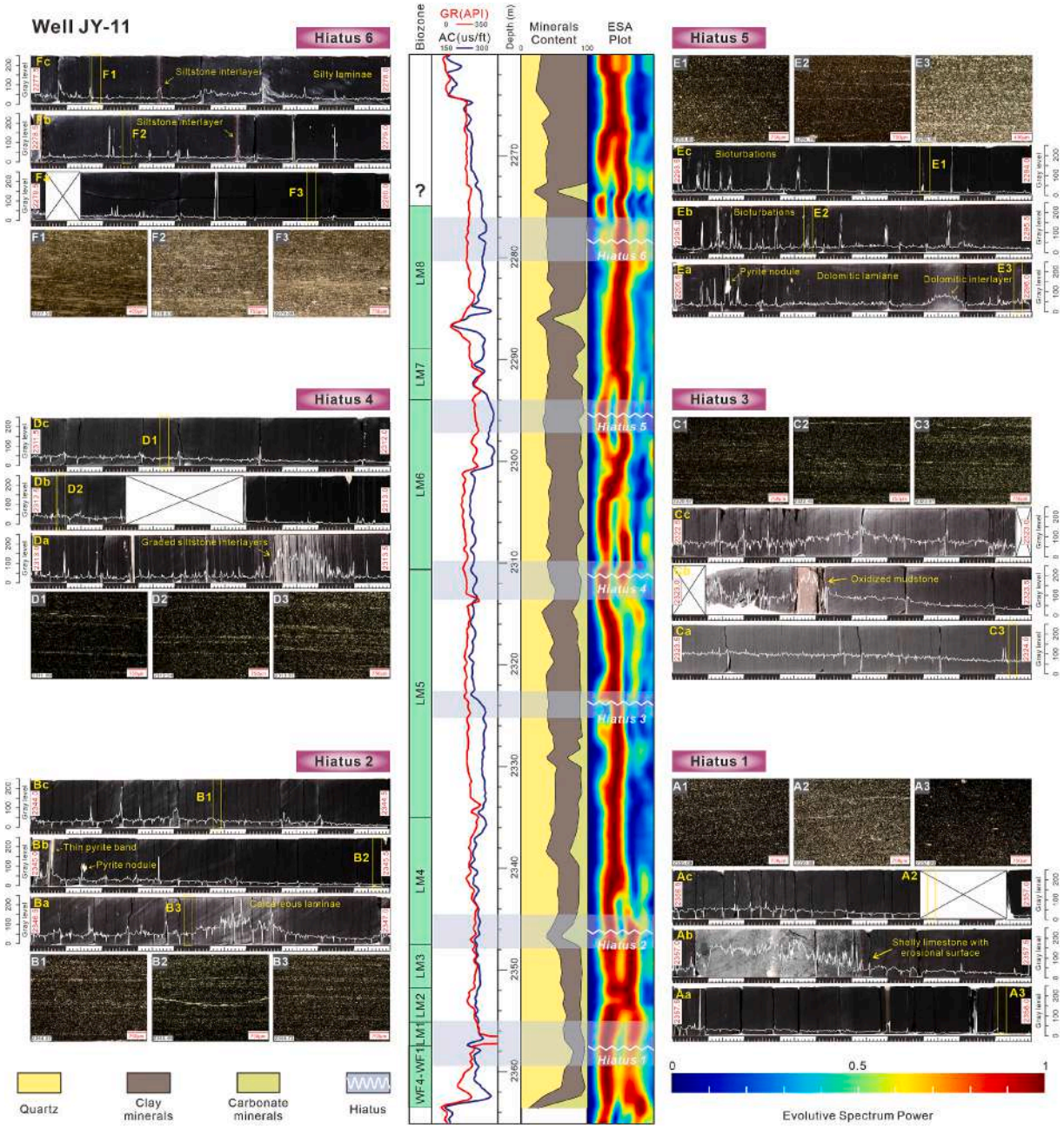

Fig. 10. Core, thin sections, and evolutive spectral analysis (ESA) evidence proximal to identified hiatuses in Well JY-11. (Aa-Ac) Core photographs near Hiatus 1: Guanyinqiao Bed shelly limestone with erosional surface overlying black shale. (A1-A3) Thin sections: Weakly developed laminae with indistinct silt layers. (Ba-Bc) Core near Hiatus 2: Increased carbonate (calcareous laminae) and minor pyrite. (B1-B3) Thin sections: Relatively high silt content and well-defined silty laminae. (Ca-Cc) Core near Hiatus 3: Oxidized purplish-red mudstone interlayer and lightened black shale. (C1-C3) Thin sections: Prominent laminated structures. (Da-Dc) Core near Hiatus 4: Increased siltstone interlayers with normal grading and silty laminae. (D1-D3) Thin sections: Distinct laminations dominated by silt. (Ea-Ec) Core near Hiatus 5: Enhanced bedding-parallel bioturbations. (E1-E3) Thin sections: Weak, discontinuous, indistinct laminae (potential bioturbation). (Fa-Fc) Core near Hiatus 6: Siltstone interlayers with flat bases within argillaceous claystone. (F1-F3) Thin sections: Clay floccules, laminated fabric defined by bedding-parallel carbonaceous laminae and floccules. (For interpretation of the references to color in this figure legend, the reader is referred to the web version of this article.)

Table 1
Mineralogical composition (wt%) and silt content (wt%) across hiatus intervals (H1-H6) in the studied sedimentary succession, with associated graptolite biozone changes.

Hiatus	Depth (m)	Quartz (%)	Clay Min. (%)	Carb. Min. (%)	I/S Mixed-Layer (%)	Illite (%)	Chlorite (%)	Silt (%)	Graptolite Zone
H1	2357.69	79	17	4	55	35	10	29	–
	2356.86	65	30	5	61	28	11	51	WF4-LM1
	2355.69	64	25	11	53	39	8	29	–
H2	2346.72	37	22	41	58	26	16	51	–
	2345.49	49	30	21	49	34	17	59	LM3-LM4
	2344.37	56	28	16	55	34	11	62	–
H3	2324.71	40	49	11	40	31	29	61	–
	2323.97	42	47	12	48	25	27	71	–
	2322.45	39	51	10	38	27	35	64	–
H4	2313.67	49	38	13	48	31	21	69	–
	2312.54	51	38	11	52	28	20	63	LM5-LM6
	2311.69	44	47	9	47	31	22	63	–
H5	2295.95	32	53	15	52	22	26	39	–
	2295.19	36	59	5	45	25	31	19	LM6-LM7
	2293.85	37	54	9	53	30	17	41	–
H6	2279.89	40	57	3	44	31	25	13	–
	2278.63	38	60	2	38	28	34	13	LM8?
	2277.59	41	57	2	55	25	20	9	–

%) contents. The clay fraction is dominated by Illite-smectite mixed-layer (I/S) (53–61 %), followed by illite (28–39 %) and minor chlorite (8–11 %).

Hiatus 2 (H2), aligned with the *LM3-LM4* transition, features well-developed pyrite and a pronounced carbonate spike (up to 41 % at 2346.72 m), manifesting as lighter calcareous laminae within black shales (Fig. 10 Ba). Thin sections display high, consistent silt fraction (51–62 %) with sharp-based muddy-silty laminae exhibiting increased thickness (Fig. 10 B1—B3). Quartz fluctuates markedly (37–56 %), with subordinate clay minerals (22–30 %). I/S (49–58 %) dominates the clay assemblage over illite (26–34 %) and chlorite (11–17 %).

Hiatus 3 (H3), unassociated with biozone boundaries, is distinguished by a distinctive purplish-red oxidized mudstone interlayer (~2323.2 m) within deepwater black shales against an elevated grayscale background (Fig. 10 Cb). Thin sections confirm uniformly high silt (61–71 %) and distinct silty laminae with increasing density towards the hiatus (Fig. 10 C1—C3). Mineralogy is clay-dominated (47–51 %), with reduced quartz (39–42 %) and low carbonate (10–11 %). I/S decreases (38–48 %) within the clay fraction, while chlorite increases significantly (27–35 %) exceeding illite (25–31 %).

Proximal to the *LM5-LM6* boundary, Hiatus 4 (H4) exhibits increased siltstone interlayers with normal-to-inverse grading (Fig. 10 Da). Very fine sand components appear near the hiatus, with high silt content (63–69 %) forming stable laminae (Fig. 10 D1—D3). Mineralogy is uniform, featuring comparable quartz (44–51 %) and clay (38–47 %) contents, plus lower carbonates (9–13 %). I/S (47–52 %) dominates the stable clay assemblage alongside illite (28–31 %) and chlorite (20–22 %).

At the *LM6-LM7* transition, Hiatus 5 (H5) displays intensified bioturbation structures (Fig. 10 Eb and 10Ec) and increased silt-rich horizontal laminae, including high-grayscale dolomitic interlayers (Fig. 10 Ea). Thin sections reveal weakly developed, often discontinuous silty laminae (Fig. 10 E1-E3). Clay minerals dominate (53–59 %), quartz decreases significantly (32–37 %), and carbonates are low and variable (5–15 %). I/S (45–53 %) dominates the clay mineral assemblage, with reduced illite (22–30 %) and increased chlorite (17–31 %).

The relationship of Hiatus 6 to the contested *LM8* Biozone top remains unresolved. Core observations document increased flat-based siltstone interlayers (Fig. 10 Fb and 10Fc). Thin sections reveal clay-rich floccules containing minor fine silt, forming elongated bedding-parallel features (Fig. 10 F1—F3), with poorly defined silty laminae and minimal silt (9–13 %). Clay minerals dominate (57–60 %), with low quartz (38–41 %) and near-absent carbonates (1–3 %). I/S fluctuates markedly (38–55 %) but dominates the clay fraction over stable illite (25–31 %) and variable chlorite (20–34 %).

4.3.3. Geochemical characteristics of hiatus

Bulk geochemical analysis of the Long-1 Member documents distinct proxy ranges (Fig. 11): Zr/Al (0.0012–0.0038; mean = 0.0024); CIA (58.2 to 74.3; mean = 64.8); Mo_{EF} (2.8–255.2; mean = 39.4); U_{EF} (1.0–36.3; mean = 5.4); Mo_{auth}/U_{auth} (0.94–4.67; mean = 2.61); Mo_{auth}/TOC (0.9–24.84; mean = 10.79); and TOC/TS (0.16–10.6; mean = 1.59). Each hiatus exhibits unique geochemical signatures compared to adjacent strata (Table 2).

Hiatus 1 (2359.06–2354.52 m) shows moderately increasing Zr/Al (0.0023–0.0025) and low CIA (58.9–62.5). Mo_{EF}-U_{EF} covariation indicates persistently euxinia (Fig. 12A). Decreasing Mo_{auth}/U_{auth} coupled with increasing TOC/TS suggests a transient oxygenation event, while a Mo_{auth}/TOC peak (21.7) implies weaker water-mass restriction (Figs. 11 and 12B).

Hiatus 2 (2347.70–2343.25 m) exhibits stable, moderately elevated Zr/Al (0.0029–0.0031) and CIA (60.3–61.1). Mo_{EF}-U_{EF} covariation indicates anoxic to weakly euxinic conditions (Fig. 12A). Increased Mo_{auth}/U_{auth} and decreased TOC/TS reflect intensification and expansion of bottom water euxinia, with higher Mo_{auth}/TOC signifying weaker marine restriction (Figs. 11 and 12B).

Hiatus 3 (2326.26–2320.97 m) is marked by a significant Zr/Al increase (up to 0.0032) against stable background and slight CIA declines (63.8–61.5). Mo_{EF}-U_{EF} suggests suboxic to anoxic conditions (Fig. 12A). Increased Mo_{auth}/U_{auth} and decreased TOC/TS reflect fortified euxinia, though a Mo_{auth}/TOC peak (13.9) denotes weaker restriction than adjacent strata (Figs. 11 and 12B).

Hiatus 4 (2314.81–2310.85 m) features Zr/Al rises to maximum 0.0033 and slight CIA decrease. Mo_{EF}-U_{EF} indicates suboxic to weakly anoxic conditions (Fig. 12A). Increased Mo_{auth}/U_{auth} and decreased TOC/TS suggest minor euxinia intensification, with a Mo_{auth}/TOC maximum (7.4) reflecting strong restriction (Figs. 11 and 12B).

Hiatus 5 (2297.12–2292.68 m) is featured by moderately low Zr/Al (0.0013 at hiatus) and significantly elevated CIA (peak 69.2). Mo_{EF}-U_{EF} evidence anoxic conditions (Fig. 12A). Increased Mo_{auth}/U_{auth} and decreased TOC/TS, coupled with Mo_{auth}/TOC declining to 10.0, indicating stronger restriction (Figs. 11 and 12B).

Hiatus 6 (2281.15–2276.55 m) displays highly variable Zr/Al (peak 0.0031 at hiatus) and a significantly elevated CIA. Mo_{EF}-U_{EF} covariation indicates suboxic to anoxic conditions (Fig. 12A). Low Mo_{auth}/U_{auth} (2.0) and reduced TOC/TS characterize the hiatus, while a significant Mo_{auth}/TOC increase (24.8) maintains a weakly restricted signature (Figs. 11 and 12B).

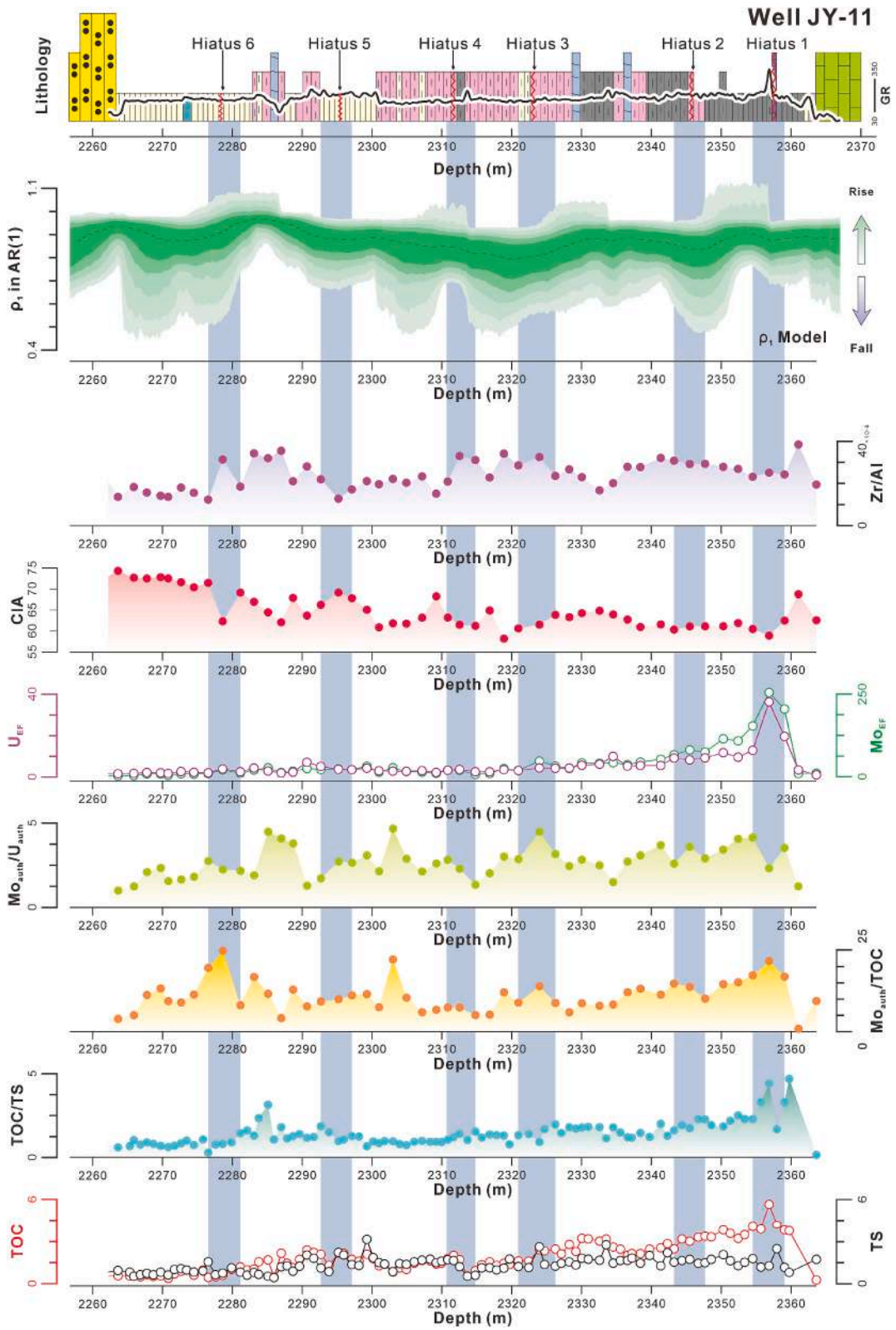

Fig. 11. Relative sea-level change recovered from the sedimentary noise modeling (ρ1 model) and geochemical proxies proximal to identified hiatuses in Well JY-11.

5. Discussion

5.1. Astrochronology and eustatic assessment of the Rhuddanian–Aeronian periods

In this study, the identification and calibration of 405 kyr long eccentricity cycles adhere to the Paleozoic astronomical timescale established by Wu et al. (2023). The results demonstrate consistent sedimentary cycles across the three studied wells, suggesting cyclic sedimentation driven by Milankovitch-scale orbital forcing. Our astrochronological analysis determined the duration of the Long-1 Member (Rhuddanian–Aeronian) as 4.45 Myr in Well JY-3, 4.43 Myr in Well JY-

Table 2
Geochemical parameters across hiatus intervals (H1-H6), showing values from below (Lower), within (Hiatus), and above (Upper) each hiatus surface.

–	Position	Depth(m)	Zr/Al	CIA	Mo_{EF}	U_{EF}	Mo_{auth}/U_{auth}	TOC/TS	Mo_{auth}/TOC
H1	Lower	2359.06	0.0024	62.5	205.0	19.6	3.5	3.2	16.9
	Hiatus	2356.86	0.0025	58.9	255.2	36.3	2.3	4.4	21.7
	Upper	2354.52	0.0023	60.5	154.2	12.9	4.2	2.3	17.3
H2	Lower	2347.70	0.0029	61.1	75.2	9.2	2.9	2.3	10.1
	Hiatus	2345.49	0.0029	61.1	81.4	8.2	3.6	1.7	13.7
	Upper	2343.25	0.0031	60.3	66.8	9.2	2.6	1.6	14.8
H3	Lower	2326.26	0.0024	63.8	32.7	4.2	3.2	2.0	8.8
	Hiatus	2323.97	0.0032	61.5	47.8	4.4	4.5	0.9	13.9
	Upper	2320.97	0.0029	60.6	19.7	3.1	2.9	1.3	8.9
H4	Lower	2314.81	0.0031	61.2	7.4	2.5	1.3	1.5	5.1
	Hiatus	2312.54	0.0033	61.5	20.0	3.7	2.3	1.4	7.4
	Upper	2310.85	0.0021	63.2	20.1	3.2	2.8	1.1	7.4
H5	Lower	2297.12	0.0017	67.8	21.9	3.5	2.6	1.3	11.1
	Hiatus	2295.19	0.0013	69.2	24.0	3.7	2.7	1.0	10.0
	Upper	2292.68	0.0022	66.2	22.8	5.1	1.7	1.9	9.3
H6	Lower	2281.15	0.0018	69.1	11.3	2.5	2.2	1.5	8.13
	Hiatus	2278.63	0.0031	62.3	21.2	3.9	2.2	0.8	24.8
	Upper	2276.55	0.0012	71.5	9.9	2.0	2.7	0.3	19.6

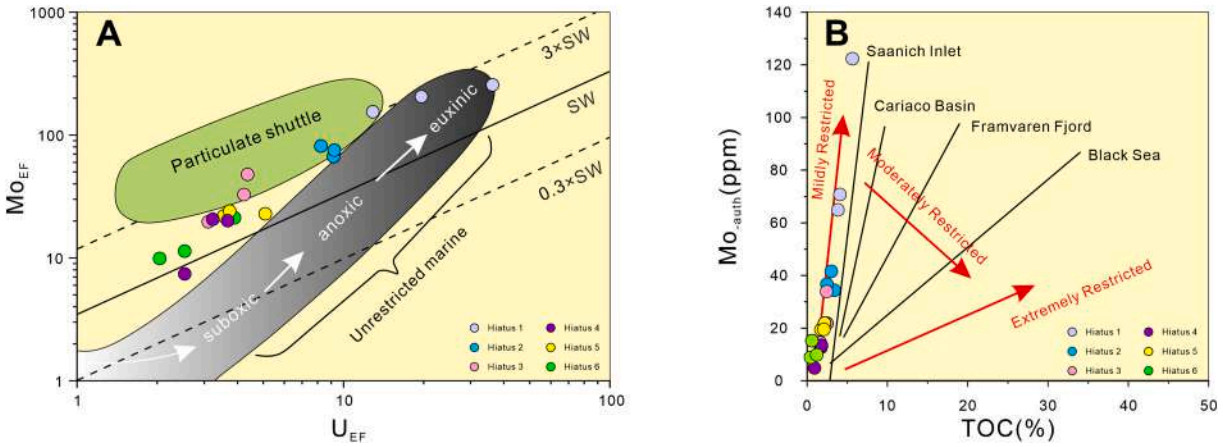

Fig. 12. Paleoredox and water mass restriction proxies near hiatuses. (A) Enrichment factors (EFs) of Mo versus U reflecting redox conditions (modified from Algeo and Tribovillard, 2009). (B) Mo_{auth}/TOC reflecting the degree of water mass restriction (modified from Algeo and Lyons, 2006; Tribovillard et al., 2012).

11, and 4.57 Myr in Well JY-51 (Fig. 7A-7C). These durations exceed the corresponding age span in GTS2020 (4.48 Myr). The slight discrepancy between our astronomical timescale and GTS2020 may reflect inherent uncertainties within the global timescale. However, Wu et al. (2023) identified 13 long eccentricity cycles during the Rhuddanian–Aeronian interval (spanning 5.27 Myr; see Fig. 2C, column 'Silurian ATS'), whereas our study recognized only 12 cycles (Fig. 3). This difference is likely attributable to the different definition of the Long-1 Member top boundary employed by Wu et al. (2023).

The relative sea-level (RSL) curve reconstructed for the Yangtze Platform by Liu et al. (2017) exhibits a high degree of concordance with the curve derived from sedimentary noise modeling (Fig. 8B and C). Both approaches reveal four major regressive events during the Rhuddanian-Aeronian stages, which correspond to recognized sedimentary hiatuses. This correspondence indicates a direct linkage between sea-level lowstands and the formation of hiatuses. However, comparison with the global eustatic curve reveals a key discrepancy (Haq and Schutter, 2008): a pronounced sea-level fall occurred on the Yangtze Platform at approximately 441.5 Ma, coinciding with a global sea-level highstand (Fig. 8D). We interpret this event as a regional regression triggered by tectonic uplift associated with the Kwangsian Orogeny (Xu et al., 2016; Yang et al., 2019; Lu et al., 2023). This observed decoupling between Yangtze Platform RSL change and global eustasy during the Early Silurian highlights the combined influence of Kwangsian Orogeny tectonism and climatic fluctuations on third-order relative sea-level variations (Munnecke et al., 2010; Boulila et al., 2011, 2020; Li et al., 2023). At the scale of fourth-order sea-level cycles, the strong agreement between the astronomically tuned age framework established in this study and those of GTS2020 and Wu et al. (2023) supports astronomically driven climate change as the primary forcing mechanism (Fig. 7A-7C).

5.2. Comprehensive interpretation of hiatuses

5.2.1. Sedimentary environment of the Wufeng-Longmaxi Formations

During the Early Silurian, the Yangtze Platform was characterized by an epicontinental sea with a platform–slope–basin morphology (Chen et al., 2014; Yang et al., 2020; Wang et al., 2023a, 2023b). The intensification of Kwangsian Orogeny during the deposition of Long-1 Member triggered a persistent relative sea-level fall, enhanced hydrodynamic conditions, and increased terrigenous input, thereby disrupting the living environment of silica-rich plankton in the ocean. As a result, the Long-1 Member exhibits a general upward increase in clay content, accompanied by a decrease in biogenic quartz and TOC. This overall trend was further modulated by higher-frequency orbital forcing (Liu et al., 2017; Jin et al., 2020; Yang et al., 2021; Lu et al., 2023).

The lower Long-1 Member was deposited in a deep-water shelf setting (Nie et al., 2024). In addition to pelagic and hemipelagic settling, energetic bottom currents and gravity flows significantly influenced fine-grained sedimentation (Lu et al., 2020; Beelen and Wood, 2023).

The upper part transitions into a shallow-water shelf environment, where wave, tidal, storm, and flood processes became frequent (Bhattacharya and MacEachern, 2009; Liang et al., 2012; Liang et al., 2016; Zhao et al., 2016; Wang et al., 2019a). In both settings, these dynamic processes led to substantial reworking and redeposition of fine-grained sediments, as well as depositional hiatuses due to erosion or non-deposition.

Sedimentary structures and geochemical proxies further elucidate the erosional or non-depositional origins of hiatuses within the Long-1 Member. Representative petrographic features proximal to hiatal surfaces are shown in Fig. 10. Detailed core examination of Long-1 Member revealed submarine erosional surfaces (H1), increasing muddy-silty laminae (H2), oxidation-induced color (H3), normal-to-inverse graded siltstone interlayers (H4), bioturbation structures (H5), and sharp-based siltstone interlayers (H6) indicating disturbances caused by bottom currents, gravity flows, or storm currents. The observations suggest heightened hydrodynamic activity near erosional hiatus surfaces or intervals associated with non-depositional events characterized by extremely low sedimentation rates.

5.2.2. Genetic mechanisms of hiatus

This study documents a series of hiatuses (H1-H6) within the Long-1 Member, revealing their genesis through the complex interplay of eustatic fluctuations, marine redox changes, and event-driven hydrodynamic processes. Integrated analysis of core lithologies, evolutive spectral analysis, mineralogical assemblages, geochemistrical proxies, regional geology, and graptolite biostratigraphy enables a systematic diagnosis of their formative mechanisms (Fig. 13A). A comparison of these hiatuses with the relative sea-level (RSL) curve derived from sedimentary noise modeling reveals that all but H5 (formed during a sea-level highstand/stillstand) correlate strongly with significant RSL lowstands, implicating regional RSL fluctuations on the Yangtze Platform as a primary driver of hiatus formation.

Hiatus 1 (H1) corresponds to the pronounced sea-level fall during the Hirnantian glaciation (Li et al., 2017a; Liu et al., 2017; Lu et al., 2020). Its boundary aligns with the transition between graptolite biozones *WF4* and *LM1*, proximal to the commonly termed "Guanyinqiao Bed"—a transitional unit between the Wufeng and Longmaxi Formations characterized by abundant *Hirnantia* fauna fossils, typically less than 0.5 m thick, and interpreted as a product of the lowstand during the Hirnantian glaciation (Lu et al., 2020; Nie et al., 2024). Core observations reveal shallow-water gray shelly limestone overlying black siliceous shale, with a distinct high-energy erosional basal surface marking an abrupt environmental shift. A significant increase in silt content near the hiatus confirms epsodic high-energy events. The shale mineralogy exhibits relatively high quartz and low clay mineral content. This high-quartz, high-silt, low-clay assemblage, coupled with elevated Zr/Al, suggests enhanced terrigenous clastic input and intense hydrodynamic winnowing during hiatus formation (Sageman et al., 2003; Tribovillard et al., 2006). Reduced CIA indicates diminished chemical weathering intensity, potentially associated with cold, arid climatic conditions (Nesbitt and Young, 1982). Mo_{EF}-U_{EF} covariation confirms deposition of surrounding fine-grained strata under strongly euxinic conditions. However, significantly elevated TOC/TS, alongside decreasing Mo_{auth}/U_{auth} and increasing Mo_{auth}/TOC, may reflect a short-term weakening of euxinic conditions and record a transient oxygenation event interrupting persistent euxinia, implying reduced marine restriction (Algeo and Lyons, 2006; Abdi et al., 2021). In summary, H1 may reflect the impact of the significant Hirnantian regression on the Yangtze Platform shelf: a substantial fall in sea level result in a marked reduction in bathymetry and induce an extensive shift in shoreline position (Hemmesch et al., 2014). Therefore, shallowing caused widespread subaerial exposure on the shelf and generated an erosional surface subsequently overlain by shelly limestone, with the contact stratigraphically recorded as a hiatus. Following deglaciation, a major transgression restored strongly euxinic conditions, resuming black shale deposition.

Hiatus 2 (H2) formed in response to the first significant Rhuddanian sea-level fall, as reconstructed from sedimentary noise modeling. Its boundary occurs near the *LM3-LM4* graptolite biozone transition. Unlike H1, no obvious physical erosional features are observed in the core; lithologically, it manifests as an abrupt change from siliceous claystone to mixed claystone/mudstone. Well-developed pyrite and light-colored calcareous laminae in the core, coupled with increased silt content and persistent silt laminae may suggest reletively high-energy events and bottom current activity in deep water (Schieber and Baird, 2001; Schieber and Riciputi, 2004; Schieber et al., 2007; Yawar and Schieber, 2017; Paz et al., 2022; Lu et al., 2023). Gradually increasing Zr/Al indicates enhanced terrigenous input and active current scouring (März et al., 2011; Bahr et al., 2014). Reduced CIA implies weakened chemical weathering due to intensified cold, arid climate. Carbonate content increases sharply near the hiatal surface (41 %), potentially signifying a regression-triggered surge in carbonate productivity or long-distance transport of shallow-water platform sediments into the deep basin by bottom current or gravity flow (Puga-Bernabéu and Betzler, 2008; Radley, 2008; Hemmesch et al., 2014). However, the presence of well-preserved planer calcareous laminae favors deposition by bottom currents (Stow and Smillie, 2020). Mo_{EF}-U_{EF} indicates anoxic to weakly euxinic conditions (Algeo and Tribovillard, 2009). Furthermore, elevated Mo_{auth}/TOC and decreased TOC/TS reflect reduced environmental restriction and increased oxygenation, leading to poorer organic matter preservation (Algeo and Lyons, 2006; Gambacorta et al., 2016; Abdi et al., 2021). Therefore, H2 formation is attributed to sea-level fall prompting basinward migration of shallow-water carbonate platforms, coupled with enhanced cold-climate bottom currents transporting platform-derived carbonates and oxygen into deep water. Active bottom current likely induced short-term seafloor erosion or non-deposition, generating the stratigraphic gap.

Hiatus 3 (H3) formed during the second significant Rhuddanian sea-level fall but lacks an associated graptolite biozone change. It is marked by a reddish mudstone interlayer, indicating oxidizing conditions within the deep-water black shale successions. The sedimentation rate curve reconstructed by eCOCO shows a significant decrease near hiatus H3 (Fig. 6B). Strata near H3 exhibit relatively high, stable clay mineral content, lower quartz content, and a lithological shift from mixed mudstone to clay-rich mudstone. The co-occurrence of increased silt content and elevated Zr/Al suggest enhanced hydrodynamics and terrigenous input (Olde et al., 2015; de Castro et al., 2021). A substantial increase in the proportion of chlorite relative to illite within the clay fraction, alongside a decrease in I/S, strongly indicates enhanced physical weathering in the source area. Reduced CIA corroborate this interpretation and indicate attenuated chemical weathering, possibly linked to brief climatic cooling (Ding et al., 2024). Mo_{EF}-U_{EF} covariation indicates surrounding shales were deposited under overall weakly anoxic conditions. Significantly increased Mo_{auth}/TOC and markedly decreased TOC/TS, combined with the presence of reddish oxidized mudstone, collectively reveal that sea level fall not only delivered detrital material but also likely carried dissolved oxygen, briefly disrupting the overall reducing environment. Therefore, H3 resulted from sea-level fall triggering brief shelf exposure and oxygenation. The transient oxygenation promoted reddish mudstone formation. Regression brought source areas closer, enabling river-delta systems to advance basinward, delivering abundant terrigenous clay and silt. Subsequently, rapid transgression likely drowning this short-lived oxidized interface and rapidly reestablished the black shale depositional environment. Moreover, a coincident stratigraphic gap evidenced by missing biostratigraphic zones suggests a potential tectonic trigger for hiatus formation linked to the intensified Kwangsian Orogeny (Cai et al., 2023).

Hiatus 4 (H4) formed during the first significant early Aeronian lowstand, its boundary near the *LM5-LM6* graptolite biozones division. A core characteristic is the increased occurrence of siltstone interlayers with normal-inverse grading; furthermore, very fine sand fractions

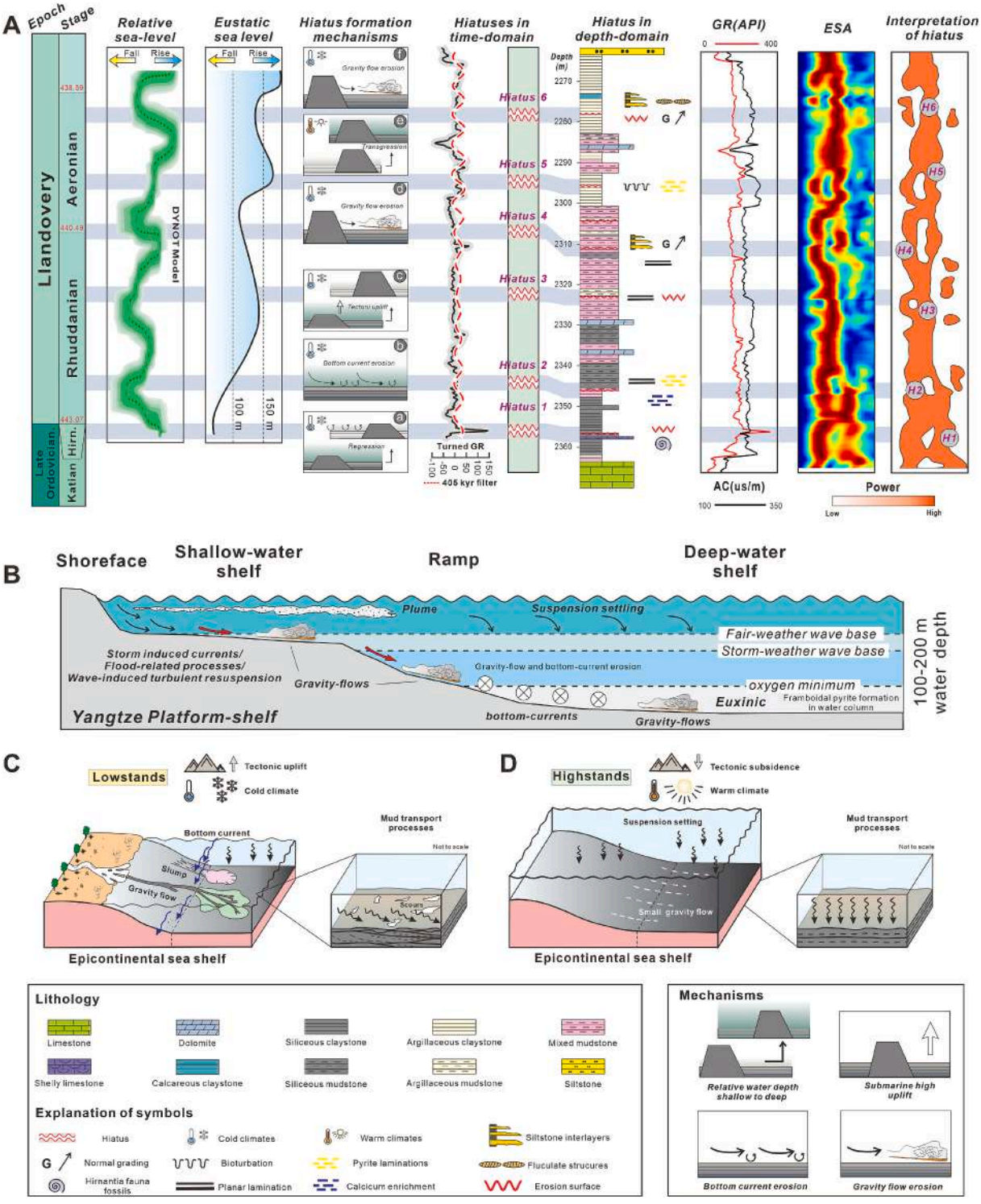

Fig. 13. Hiatus characteristics and formation mechanisms in the Long-1 Member (Well JY-11). (A) Stratigraphic overview of hiatuses and interpreted mechanisms: Hiatus 1 - Shelf exposure/related gravity/bottom current erosion during major icehouse sea-level fall; Hiatus 2 - Enhanced bottom current erosion/reworking (cold climate); Hiatus 3 - Enhanced bottom current erosion/reworking (tectonic uplift); Hiatus 4 - Enhanced gravity-flow erosion (Rhuddanian-Aeronian transition); Hiatus 5 - Sediment starvation and bioturbation associated with relative shallowing then deepening; Hiatus 6 - Enhanced gravity-flow erosion (cold climate). (B) Generalized model for the Long-1 Member showing hydrodynamic processes for generating hiatuses. The Long-1 Member likely persisted in a persistently subaqueous setting characterized by a euxinic to suboxic water column throughout its depositional history. However, episodic gravity flows and bottom currents may have introduced oxygenated waters, generating transient oxygenation events within this otherwise reducing environment (modified from Loucks and Ruppel, 2007). (C, D) Conceptual models of hiatus development relative to relative sea-level (RSL). Bottom current velocity and gravity-flow erosion potential increase during RSL lowstands, favoring erosional hiatuses and specific structures (scours, lenticular bedding, floccules). During highstands, suspension settling dominates, reducing erosion potential but increasing likelihood of non-deposition hiatuses due to sediment starvation. Legend partially modified from Schieber and Shao (2021).

appear for the first time near the hiatus surface, potentially indicating enhanced fine-grained sediment gravity flows (Zavala and Arcuri, 2016; Boulesteix et al., 2020; Yang and Liu, 2025). Stable quartz content, high silt content with resulting stable laminae, and elevated Zr/Al confirm episodic high-energy flow regimes and sustained terrigenous clastic input (Ondřej et al., 2018). Reduced CIA reflects weakened chemical weathering in the source area, possibly corresponding to brief climatic cooling. Mo_{EF}-U_{EF} indicates overall enhanced oxygenation (suboxic to weakly anoxic conditions). Therefore, H4 formation is related to shelf exposure during sea-level fall and enhanced gravity flow events, where sediment bypass by gravity flows likely create an erosional hiatus.

Hiatus 5 (H5) corresponds to an Aeronian sea-level rise/stillstand, its boundary at the *LM6-LM7* graptolite biozones transition. Core characteristics show significant bioturbation, predominantly comprising horizontal burrows parallel to bedding, indicating relatively weak hydrodynamics (Dashtgard and MacEachern, 2016; Lu et al., 2020). Enhanced bioturbation reflects a low-energy, episodically oxidized and more hiabitable environment (Aller, 1994; Hickey and Henk, 2007; Dashtgard and MacEachern, 2016; Li et al., 2017b). Biological reworking disrupted primary laminae continuity and decomposed sedimentary organic matter (Jin et al., 2020). Combined with highly fluctuating silt content (e.g., a sharp drop to 19 % at 2295.19 m) and very low Zr/Al near the hiatus, this suggests slow sedimentation rates in a low-energy setting with limited coarse-grained clastic input and destruction of primary bedding by benthic activity (Zeller et al., 2015; Schimmelmann et al., 2016). Mineral composition is clay-dominated, with a sharp decrease in quartz, indicating a fine-grained, clay-rich, low-energy depositional environment, potentially accompanied by intensified influx of fine-grained sediments. Consistently high CIA denotes intense source area chemical weathering, reflecting a significantly warm, humid climate and likely elevated sea levels. Low Zr/Al coexisting with high CIA suggests chemical weathering dominated under warm and humid conditions, which greatly reduced the supply efficiency of terrigenous material, resulting in terrigenous input dominated by fine-grained weathered clays with limited coarse clastic transport. Mo_{EF}-U_{EF} covariation reflects suboxic to weakly anoxic water conditions, with increased anoxia compared to Hiatus 4, indicating a restoration of environmental reductivity, potentially related to absolute sea-level rise. Relatively stable Mo_{auth}/TOC suggests strongly restricted water mass conditions. Low TOC/TS reflects periodic weak oxygenation events at the sediment-water interface, promoting organic matter degradation. Consequently, H5 did not result from any erosive event but likely resulted from sediment starvation and bioturbation under low sedimentation rates during sea-level rise/stillstand under humid climate conditions; low silt content and weakly developed laminae indicate extremely low terrigenous input, which promoted enhanced benthic reworking compromising stratigraphic preservation.

Hiatus 6 (H6) corresponds to a significant end-Aeronian lowstand. The core interval near H6 is characterized by abrupt, flat-based siltstone interlayers suggestting scouring by gravity flows disrupted the sedimentary succession (Liang et al., 2016; Al-Mufti and Arnott, 2024). Mineralogically, clay mineral dominance and low silt content reflect an overall low-energy, quiet-water depositional background. Thin sections reveal elongated clay-silt floccules along bedding planes, potentially indicating erosive currents and bedload transport of muds associated with fine-grained sediment gravity flows (Schieber, 2016; Li et al., 2017a, 2017b). A sharp increase in Zr/Al reflects pulsed input of coarse-grained terrigenous clastics, implying anomalous hydrodynamic events (possibly surge-type gravity flows; Liang et al., 2012; Yang et al., 2024). Significantly reduced CIA suggests a sudden weakening of chemical weathering intensity, possibly linked to brief cold climate conditions. Mo_{EF}-U_{EF} covariation indicates suboxic depositional waters, while significantly increased Mo_{auth}/TOC and decreased TOC/TS reflect rapid reduction in marine restriction and increased oxygenation. In summary, H6 may be related to gravity flows triggered by a brief cold climate episode: cooling induced significant sea-level fall and frequent gravity flows, whose erosive currents scoured underlying strata, causing an interruption in the sedimentary record.

Although geochemical indicators show predominantly euxinic to suboxic conditions during most of the Long-1 Member deposition, diagnostic features signaling short-term oxygenation events mark hiatus–associated surfaces. Furthermore, persistently high silt content and well-developed laminae near most hiatuses implay significant erosion and reworking by bottom currents and/or gravity flows across the shelf environment (Fig. 13B, Wilson and Schieber, 2015; Liang et al., 2016; Yawar and Schieber, 2017; Lu et al., 2023). However, conventional recognition of erosional surfaces within fine-grained successions is frequently problematic in core due to their characteristically sub-horizontal geometries (Schieber, 2003; Hemmesch et al., 2014). The co-occurrence of elevated Zr/Al and reduced CIA indicates enhanced terrigenous clastic input, cool climatic conditions, and high-energy hydrodynamic regimes during hiatus development.

Notably, most hiatus exhibit significantly higher Mo_{auth}/U_{auth}, lower TOC/TS, and higer Mo_{auth}/TOC ratios relative to underlying strata. This geochemical signature suggests conditions favoring Mo enrichment and intensified water-column sulfidation coinciding with hiatus occurrence (Fig. 13B). This pattern is most consistently explained by enhanced terrigenous nutrient input during sea-level lowstands. The increased flux of nutrients likely stimulated primary productivity, which would have promoted oxygen consumption through organic matter respiration, potentially resulting in the development of euxinic conditions within the water column.

Overall, periodic RSL fluctuations, driven by glacio-eustasy and local tectonics, fundamentally control hiatus development by modulating terrigenous input, marine redox conditions, and primary paleoproductivity (Vahlenkamp et al., 2018; Catuneanu, 2022; Tagliaro et al., 2022; Zhang et al., 2023a, 2023b; Li et al., 2024). These represent the principal allogenic control, though stochastic events (e.g., slumping, earthquakes) may cause localized deviations (van der Merwe et al., 2010; Arai et al., 2013; Boulesteix et al., 2020). Such controls ultimately regulate basin-wide base-level changes and hiatus-forming mechanisms.

A theoretical model for sedimentary hiatus formation is proposed (Fig. 13C-13D). Mechanistically, RSL lowstands promote significant subaerial exposure, erosion, and sediment bypass, generating regional unconformities on land (typically third-order scale or higher; Fig. 13C; Catuneanu, 2022). Contemporaneously, cold climates intensify thermohaline circulation, amplifying bottom-current erosion and sediment redistribution in subaqueous environments (Fig. 13C; Hall et al., 2001; de Boer et al., 2007; Thomas et al., 2022). Advancing deltaic systems deliver increased sediment loads to shelf margins and canyon heads, frequently triggering hyperpycnal flows and gravity-driven processes (Boulesteix et al., 2019). These along-slope and down-slope dynamics generate erosional scours, graded silty/mud laminae, and clay floccule fabrics—features diagnostic of fine-grained bedload transport that enhance hiatus probability (Fig. 13C; Schieber et al., 2007; Schieber et al., 2010; Yawar and Schieber, 2017). Conversely, during highstands, warmer climates reduce thermohaline circulation intensity, diminishing bottom-current activity and favoring suspension settling of fine-grained sediments via buoyant plumes (“lofting”). Gravity flows become less frequent and lower energy, limiting erosional hiatuses potential (Fig. 13D). However, these conditions may induce sediment starvation and condensation, often accompanied by intense bioturbation (as observed in H5).

5.3. Identification and classification scheme of Hiatus

The recognition of pervasive hiatuses has underscored the incomplete nature of fine-grained sedimentary successions across varied spatiotemporal scales (Fig. 14A; Sadler, 1999; Miall, 2016; Schieber, 2016). Hiatus formation during lowstands is frequently associated with erosion or non-deposition, whereas highstand hiatuses are commonly linked to sediment starvation. Although hiatuses in settings such as

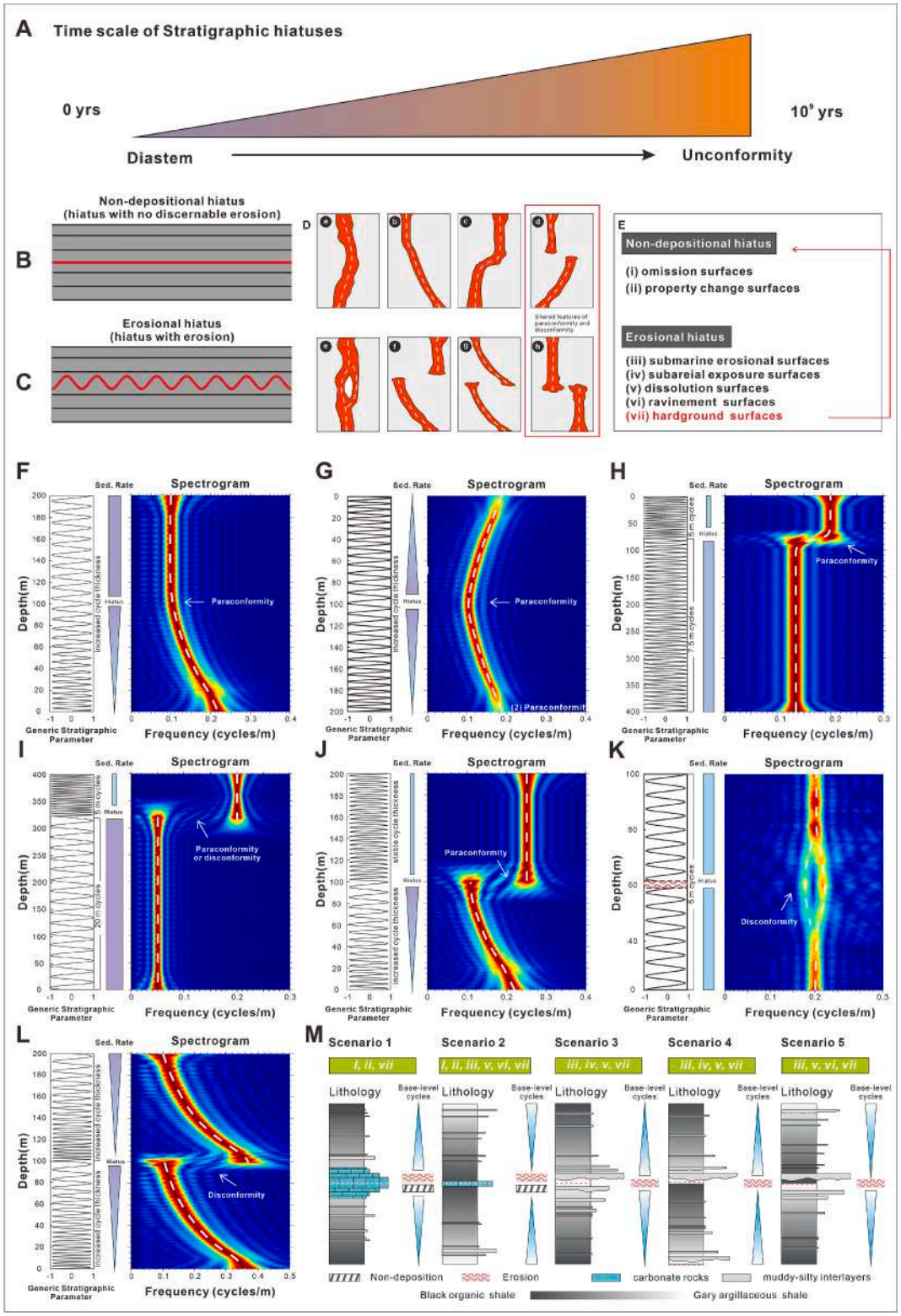

Fig. 14. Scale, classification, and detection of stratigraphic hiatuses. (A) Hierarchy of hiatus scales (modified from Catuneanu, 2022). (B-E) Classification of hiatus types and their characteristic responses in Evolutive Spectral Analysis (ESA) spectrograms. (F-M) Model simulations of hiatus scenarios showing effects in frequency domain and lithological profiles.

shoreface, tidal flat, and carbonate platforms have been well documented (e.g., Sattler et al., 2005; Christ et al., 2015; Strasser, 2015; Brady and Bowie, 2017; Wroblewski and Morris, 2023), their systematic identification within fine-grained successions remains challenging due to genetic complexity and terminological inconsistency.

Stratigraphic hiatuses are conventionally divided into two broad categories: non-depositional hiatuses, which lack erosional features and reflect reduced sedimentation, and erosional hiatuses, marked by clear evidence of sediment removal (see Fig. 14B and C; Kabanov, 2017; Catuneanu, 2022). This study demonstrates that hiatuses produce

diagnostic ESA signatures, including gradual or abrupt shifts in spectral power and bifurcated peaks (Fig. 14D and E). Building on established mechanisms, we further classify hiatuses into seven subcategories: (see Fig. 14E): (i) omission surfaces: formed near maximum flooding surfaces due to sediment starvation (Föllmi, 2016); (ii) sediment property change surfaces: marked by abrupt lithological or compositional shifts (Embry, 2009); (iii) erosional surfaces: resulting from current or density flow scouring (Stow et al., 2001; Schieber, 2016; Dutkiewicz and Müller, 2022; Ineson et al., 2022); (iv) seafloor exposure surfaces: caused by sea-level fall or tectonic uplift (Wilson and Schieber, 2014); (v) dissolution surfaces: formed by chemical corrosion of susceptible materials (Moore Jr et al., 1978); (vi) ravinement surfaces: generated by wave or tidal

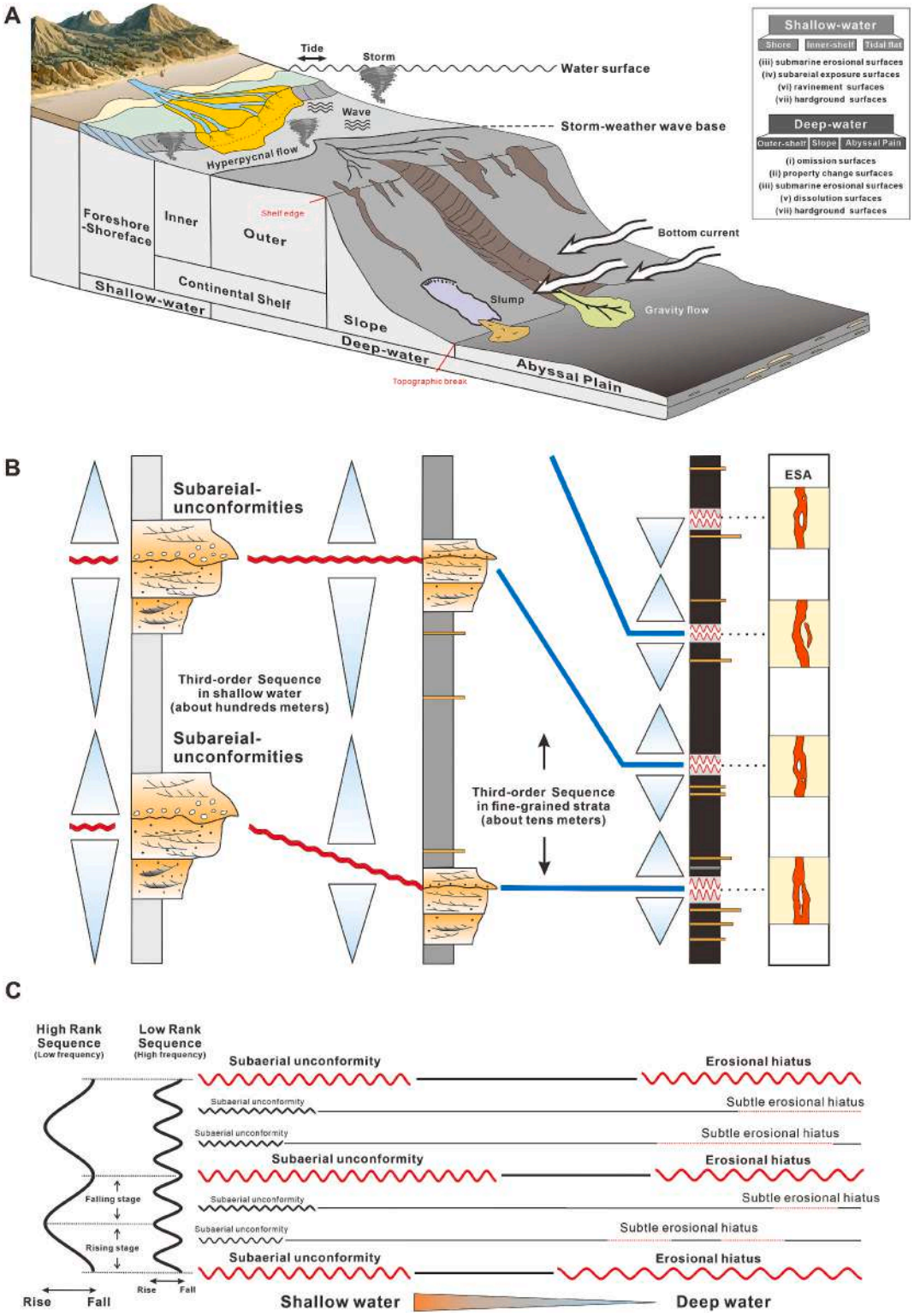

Fig. 15. Conceptual models of hiatus formation across depositional settings. (A) Sedimentary processes and hiatus types from shallow to deep marine environments. (B) Transition model from subaerial unconformities (SU) to deep-water hiatuses at the third-order sequence scale, utilizing Evolutive Spectral Analysis (ESA) for boundary identification. (C) Idealized model of SU and erosional hiatuses development controlled by different-order cycles across a shelf-to-basin profile.

erosion during transgression (Cattaneo and Steel, 2003; Catuneanu, 2022); and (vii) hardground surfaces: resulting from seafloor carbonate cementation (Christ et al., 2015).

Synthesizing this framework, this study proposes a classification scheme integrating hiatus types with diagnostic ESA spectrogram features (See Fig. 14D and E). Mechanisms generating these diagnostic features are illustrated in Figs. 14F-14L, alongside base-level change models driving hiatus formation (see Fig. 14M, Scenarios 1–5). Subcategories (i) and (ii) aligned with non-depositional hiatuses, while categories (iii), (iv), (v), and (vi) represent erosional hiatuses. Hardground surfaces (vii) exhibited attributes of both non-deposition and erosion and may be classified under either non-deposional or erosional hiatuses, depending on specific research focuses and observed sedimentary structures.

The examples presented in this study, along with the data of prior studies on fine-grained successions, indicate that during sea level fall, hiatuses within shallow-water shales are commonly manifest as exposure surfaces or erosional surfaces, associated respectively associated with subaerial exposure and erosion by gravity flows or traction currents (e.g., storms, waves, tides; Schieber, 1994; Bohacs et al., 2014; Schieber, 2016). During sea-level rise, ravinement surfaces related to transgressive wave or tidal erosion are typically developed. In contrast, in deep-water settings, only a small number of hiatuses are attributed to dissolution (Dutkiewicz and Müller, 2022). Instead, the primary mechanisms for hiatuses formation during lowstands include non-deposition (e.g., seafloor hardgrounds and sediment starvation) and mechanical scouring or sediment redistribution driven by erosive hydrodynamic and mass transport processes (e.g., bottom currents, turbidity currents, hyperpycnal flows, debris flows, wave-enhanced gravity flows, and pelagic storms; Mulder and Syvitski, 1995; Stow et al., 2001; Macquaker et al., 2007; Macquaker et al., 2010; Harris and Whiteway, 2011; Dutkiewicz et al., 2016; Azpiroz-Zabala et al., 2017; Stow and Smillie, 2020) (Fig. 15A). Consequently, the dominant hiatus types in these settings include omission surfaces, property change surfaces, erosional surfaces, and hardground surfaces.

5.4. Hierarchy of hiatuses and implications for sequence stratigraphy

The application of sequence stratigraphy to fine-grained successions is often underestimated, owing to the conventional assumption that clay- and silt-sized particles are deposited exclusively through suspension settling. However, the presence of hiatuses (both non-depostional hiatuses and erosional hiatuses), which typically serve as sequence boundaries and record key tectonic and eustatic processes, provides valuable insights into sequence subdivision (Weedon, 2003; Brady and Bowie, 2017; Kabanov, 2017). This study demonstrates that, although such hiatuses are generally small in scale, they can be identified effectively through ESA and are typically associated with RSL lowstands (except sediment starvation commonly occurs during highstand). These findings establish a basin-wide connection between proximal subaerial unconformities and distal subaqueous hiatuses, offering significant potential for refining fine-grained sequence stratigraphic frameworks (Fig. 15A and B).

Barrell (1917) proposed a pioneering one-dimension model that linked stratigraphic accumulation to base-level rise, emphasizing how the fluctuations in the base level can contribute to the formation of hiatuses. This model is more complex when examined through the lens of sequence stratigraphy, where hierarchy plays a fundamental role (Miall, 2016; Catuneanu, 2022). Generally, the changes in sea level occur across a broad spectrum of timescales, from first-order global tectonics to fifth-order Milankovitch cycles. The interplay between sea-level fluctuations of varying magnitudes and the strengthening of formative mechanisms suggests that hiatuses may be generated and recognized differently depending on the observed scale (McLaughlin et al., 2008; Miall, 2016; Stow and Smillie, 2020). Therefore, hiatuses of varying magnitudes and durations should be ranked according to scale of their controlling processes. Within the resolution of this study, the hiatuses formed by larger-scale fluctuations (e.g., third-order eustatic changes) are likely to have a more significant stratigraphic impact than those formed by higher-frequency cycles (e.g., autogenic processes, millennial-scale climatic variability, or short-term extreme events; Hilgen et al., 2015; Miall, 2016). In this content, during higher-frequency fluctuations (e.g., fourth-order, fifth-order, or even higher frequencies cycles), temporay lowstands may produce subtle hiatuses rather than prominent ones, which may not present discernible erosion features due to weak bottom currents and small-scale gravity flows (Fig. 15C). However, this insensitivity possible arises from the limited ability of basinal sections to record low-rank and small-to-moderate amplitude regressive-transgressive sea-level fluctuations, as they may not significantly affect the seafloor processes (Immenhauser and Scott, 2002). In this content, long-term climatic changes or the evolution of ocean currents over million-year scales are likely to generate detectable hiatuses in the stratigraphic records.

Overall, this study highlights the importance of RSL changes, rather than event-driven disturbances, as primary drivers of hiatus formation. Additionally, the findings suggest that hiatuses play a critical role in identifying significant sea-level lowstands and sedimentation starvation associated with highstand, potentially serving as sequence boundaries in fine-grained successions. However, whether detectable hiatuses can be observed at higher-frequency RSL cycles remains unresolved and requires further investigation.

6. Conclusions

This study systematically identified six potential stratigraphic hiatuses within the Long-1 Member in Sichuan Basin, South China, through an integrated approach combining cyclostratigraphy and fine-grained rock petrography with geophysical and geochemical datasets. The findings offer new insights into the genetic mechanisms and hierarchical nature of hiatuses in fine-grained depositional systems while providing key insights into sequence stratigraphic significance. The main conclusions can be summarized as follows:

(1) Detailed petrographic analysis revealed Long-1 Member predominantly comprises siliceous, argillaceous, and calcareous claystone/mudstones, with a distinct lithology transition from siliceous to argillaceous claystone/mudstone, indicating a gradual shallowing of the depositional environment and enhanced chemical weathering intensity. This transition was strongly influenced by the Kwangsian Orogeny, resulting in a shift from a deep-water shelf to a shallow-water shelf setting. Cyclostratigraphic analysis identified distinct astronomical cycles, such as eccentricity cycles, and provided an absolute astronomical timescale for Long-1 Member (443.1–438.6 Ma). Additionally, the sedimentary noise modeling reconstructed a robust RSL curve, which served as a solid foundation for examining the relationship between hiatus formation and RSL changes.
(2) Combining sedimentology, cyclostratigraphy, geochemistry, and Evolutive Spectral Analysis (ESA), six major hiatuses (Hiatuses 1–6) were identified within Long-1 Member. These hiatuses closely corresponded to third-order RSL lowstands and were associated with dynamic hydrodynamic conditons, such as bottom currents, gravity flows. Glacio-eustatic and tectonic factors primarily controlled these processes. Eustatic sea-level falls and regional tectonic uplifts enhanced bottom currents and gravity flows erosion, leading to the formation of prominent erosional hiatuses.
(3) By intergrating evolutive spectral analysis (ESA), this study proposed a systematic classification scheme for identifying hiatuses and deciphering their formation mechanisms in fine-grained successions. The results demonstrated that ESA is an effective tool for detecting and distinguishing subtle hiatuses. It

highlighted the spectral bifurcation and power shifts as diagnostic features to differentiate non-erosional hiatuses from erosional hiatuses. Based on different physical mechanisms, hiatuses can be further classified into seven subcategories (e.g., omission surfaces, sedimentary property change surfaces, erosional surfaces, seafloor exposure surfaces, dissolution surfaces, ravinement surfaces and harground surfaces).

(4) The hierarchy of hiatuses was closely tied to the scale of RSL fluctuations across multiple scales. Third-order cycles emerged as the primary drivers of major erosional hiatuses, while high-frequency (fourth-order and above) climatic fluctuations and local tectonic adjustments caused transient lowstands, predominantly forming more subtle and cryptic hiatuses. This hierarchical framework provides a robust foundation for subdividing fine-grained successions within the context of sequence stratigraphy. However, whether detectable hiatuses can be observed in higher-frequency sequence cycles remains unresolved and warrants further investigation.

CRediT authorship contribution statement

Yichen Liu: Writing – original draft, Investigation, Formal analysis. **Benzhong Xian:** Writing – review & editing, Supervision, Project administration, Methodology, Conceptualization. **Qianran Wu:** Writing – review & editing, Investigation, Data curation. **Zhiyong Lu:** Validation, Resources. **Haocheng Shi:** Writing – review & editing, Investigation. **Mingjin Wu:** Visualization, Formal analysis. **Zhiyun Yu:** Methodology, Investigation. **Lin Zhao:** Investigation, Formal analysis. **Junyang Geng:** Validation, Investigation. **Haiying Chen:** Writing – review & editing, Validation.

Declaration of competing interest

The authors declare that they have no competing financial interests or personal relationships that could have influenced the work reported in this manuscript. All funding sources supporting this research were clearly disclosed in the acknowledgments section, and no conflicts of interest arise from these sources. The authors affirm that affiliations with academic and industrial institutions did not bias the interpretation or presentation of the research findings.

Acknowledgments

The study presented in this paper was supported by the National Natural Science Foundation of China (grants 42172109, 41872113, and 42172108), China National Petroleum Corporation - China University of Petroleum (Beijing) strategic cooperation science and technology project (ZLZX2020-02) and Science Foundation of China University of Petroleum (Beijing) (No. 2462020BJRC002, 2462020YXZZ020). We gratefully acknowledge their support. The authors thank the Sinopec Jianghan Oilfield Branch Company for providing research materials and support. The authors would also like to extend their sincere gratitude to the anonymous reviewers for their insightful comments and constructive suggestions, which have greatly improved the quality of this manuscript.

Appendix A. Supplementary data

Supplementary data to this article can be found online at https://doi.org/10.1016/j.coal.2025.104869.

Data availability

The data that support the findings of this study are available from the corresponding author upon reasonable request.

References

Abdi, Z., Rimmer, S.M., Rowe, H.D., Nordeng, S., 2021. Controls on organic matter accumulation in the Bakken Formation, Williston Basin, USA. Chem. Geol. 586, 120588. https://doi.org/10.1016/j.chemgeo.2021.120588.

Algeo, T.J., Lyons, T.W., 2006. Mo–total organic carbon covariation in modern anoxic marine environments: Implications for analysis of paleoredox and paleohydrographic conditions. Paleoceanography 21 (1). https://doi.org/10.1029/2004PA001112.

Algeo, T.J., Tribovillard, N., 2009. Environmental analysis of paleoceanographic systems based on molybdenum–uranium covariation. Chem. Geol. 268 (3), 211–225. https://doi.org/10.1016/j.chemgeo.2009.09.001.

Aller, R.C., 1994. Bioturbation and remineralization of sedimentary organic matter: effects of redox oscillation. Chem. Geol. 114 (3), 331–345. https://doi.org/10.1016/0009-2541(94)90062-0.

Al-Mufti, O.N., Arnott, R.W.C., 2024. The origin of planar lamination in fine-grained sediment deposited by subaqueous sediment gravity flows: the Depositional. Record 10 (5), 496–514. https://doi.org/10.1002/dep2.257.

Álvaro, J.J., Clausen, S., 2006. Microbial crusts as indicators of stratigraphic diastems in the Cambrian Brèche à Micmacca, Atlas Mountains of Morocco. Sediment. Geol. 185 (3), 255–265. https://doi.org/10.1016/j.sedgeo.2005.12.007.

Ankindinova, O., Aksu, A., Hiscott, R., 2020. Holocene sedimentation in the southwestern Black Sea: Interplay between riverine supply, coastal eddies of the Rim Current, surface and internal waves, and saline underflow through the Strait of Bosphorus. Mar. Geol. 420, 106092. https://doi.org/10.1016/j.margeo.2019.106092.

Aplin, A.C., Macquaker, J.H., 2011. Mudstone diversity: Origin and implications for source, seal, and reservoir properties in petroleum systems. AAPG Bull. 95 (12), 2031–2059. https://doi.org/10.1306/03281110162.

Arai, K., Naruse, H., Miura, R., Kawamura, K., Hino, R., Ito, Y., Inazu, D., Yokokawa, M., Izumi, N., Murayama, M., 2013. Tsunami-generated turbidity current of the 2011 Tohoku-Oki earthquake. Geology 41 (11), 1195–1198. https://doi.org/10.1130/G34777.1.

Atar, E., März, C., Aplin, A.C., Dellwig, O., Herringshaw, L.G., Lamoureux-Var, V., Leng, M.J., Schnetger, B., Wagner, T., 2019. Dynamic climate-driven controls on the deposition of the Kimmeridge Clay Formation in the Cleveland Basin, Yorkshire, UK: Clim. Past 15 (4), 1581–1601. https://doi.org/10.5194/cp-15-1581-2019.

Azpiroz-Zabala, M., Cartigny, M.J., Talling, P.J., Parsons, D.R., Sumner, E.J., Clare, M.A., Simmons, S.M., Cooper, C., Pope, E.L., 2017. Newly recognized turbidity current structure can explain prolonged flushing of submarine canyons. Sci. Adv. 3 (10), e1700200. https://doi.org/10.1126/sciadv.1700200.

Bahr, A., Jiménez-Espejo, F.J., Kolasinac, N., Grunert, P., Hernández-Molina, F.J., Röhl, U., Voelker, A.H., Escutia, C., Stow, D.A., Hodell, D., 2014. Deciphering bottom current velocity and paleoclimate signals from contourite deposits in the G ulf of C ádiz during the last 140 kyr: an inorganic geochemical approach: Geochemistry. Geophysics, Geosystems 15 (8), 3145–3160. https://doi.org/10.1002/2014GC005356.

Barnett, A., Wright, V., 2008. A sedimentological and cyclostratigraphic evaluation of the completeness of the Mississippian–Pennsylvanian (Mid-Carboniferous) global stratotype section and point, Arrow Canyon, Nevada, USA. J. Geol. Soc. 165 (4), 859–873. https://doi.org/10.1144/0016-76492007-122.

Barrell, J., 1917. Rhythms and the measurements of geologic time. Bull. Geol. Soc. Am. 28 (1), 745–904. https://doi.org/10.1130/GSAB-28-745.

Barron, J.A., Keller, G., 1982. Widespread Miocene deep-sea hiatuses: Coincidence with periods of global cooling. Geology 10 (11), 577–581. https://doi.org/10.1130/0091-7613(1982)10<577:WMDHCW>2.0.CO;2.

Beelen, D., Wood, L.J., 2023. Predicting bottom current deposition and erosion on the ocean floor. Basin Res. 35 (5), 1985–2009. https://doi.org/10.1111/bre.12788.

Berger, A., Loutre, M.F., 1994. Astronomical Forcing through Geological Time. In: de Boer, P.L., Smith, D.G. (Eds.), Orbital Forcing and Cyclic Sequences, pp. 15–24. https://doi.org/10.1002/9781444304039.ch2.

Berggren, W., 1978. Recent Advances in Cenozoic Planktonic Foraminiferal Biostratigraphy, Biochronology, and Biogeography. Micropaleontology, Atlantic Ocean, pp. 337–370. https://doi.org/10.2307/1485368.

Bhattacharya, J., MacEachern, J., 2009. Hyperpycnal Rivers and Prodeltaic Shelves in the cretaceous Seaway of North America. J. Sediment. Res. 79, 184–209. https://doi.org/10.2110/jsr.2009.026.

Bohacs, K.M., Lazar, O.R., Demko, T.M., 2014. Parasequence types in shelfal mudstone strata—Quantitative observations of lithofacies and stacking patterns, and conceptual link to modern depositional regimes. Geology 42 (2), 131–134. https://doi.org/10.1130/G35089.1.

Boulesteix, K., Poyatos-Moré, M., Flint, S.S., Taylor, K.G., Hodgson, D.M., Hasiotis, S.T., 2019. Transport and deposition of mud in deep-water environments: Processes and stratigraphic implications. Sedimentology 66 (7), 2894–2925. https://doi.org/10.1111/sed.12614.

Boulesteix, K., Poyatos-Moré, M., Hodgson, D.M., Flint, S.S., Taylor, K.G., 2020. Fringe or background: Characterizing deep-water mudstones beyond the basin-floor fan sandstone pinchout. J. Sediment. Res. 90 (12), 1678–1705. https://doi.org/10.2110/jsr.2020.048.

Boulila, S., Galbrun, B., Miller, K.G., Pekar, S.F., Browning, J.V., Laskar, J., Wright, J.D., 2011. On the origin of Cenozoic and Mesozoic "third-order" eustatic sequences. Earth Sci. Rev. 109 (3), 94–112. https://doi.org/10.1016/j.earscirev.2011.09.003.

Boulila, S., Brange, C., Cruz, A.M., Laskar, J., Gorini, C., Dos Reis, T., Silva, C.G., 2020. Astronomical pacing of late cretaceous third-and second-order sea-level sequences in the Foz do Amazonas Basin. Mar. Pet. Geol. 117, 104382. https://doi.org/10.1016/j.marpetgeo.2020.104382.

Brady, M., Bowie, C., 2017. Discontinuity surfaces and microfacies in a storm-dominated shallow Epeiric Sea, Devonian Cedar Valley Group, Iowa. Depositional Rec. 3 (2), 136–160. https://doi.org/10.1002/dep2.26.
Braithwaite, C.J.R., 2020. Last Interglacial changes in sea level on Aldabra western Indian Ocean. Sedimentology 67 (6), 3236–3258. https://doi.org/10.1111/sed.12738.
Burgess, P.M., Duller, R.A., 2024. Autogenic masking of allogenic inputs: Numerical modelling of signal preservation in deep-water fan strata. Earth Planet. Sci. Lett. 628, 118583. https://doi.org/10.1016/j.epsl.2024.118583.
Cai, Q.-S., Hu, M.-Y., Kane, O.I., Yang, Z., Wen, Y.-R., Luo, Q., Li, M.-T., Hu, Z.-G., Deng, Q.-J., 2023. Petrological and geochemical characteristics of the Ordovician–Silurian black shale in eastern Sichuan and western Hubei, South China: Differential sedimentary responses to tectonism and glaciation. J. Palaeogeogr. 12 (1), 129–152. https://doi.org/10.1016/j.jop.2022.09.003.
Cao, Y., Lin, M., Xi, K., Xu, S., Zou, C., 2024. Bedload transport and deposition of mud-grade sediments in deep-lacustrine settings: a case study in the Triassic Yanchang Formation, Ordos Basin, China. Sedimentology 71 (6), 1984–2008. https://doi.org/10.1111/sed.13200.
Cattaneo, A., Steel, R.J., 2003. Transgressive deposits: a review of their variability. Earth Sci. Rev. 62 (3), 187–228. https://doi.org/10.1016/S0012-8252(02)00134-4.
Catuneanu, O., 2022. Principles of Sequence Stratigraphy, 2nd ed. Elsevier, Amsterdam, Netherlands https://www.elsevier.com/books-and-journals.
Chen, X., Zhang, Y., Fan, J., Cheng, J., Li, Q., 2010. Ordovician graptolite-bearing strata in southern Jiangxi with a special reference to the Kwangsian Orogeny. Sci. China Earth Sci. 53, 1602–1610. https://doi.org/10.1007/s11430-010-4117-6.
Chen, X., Fan, J., Chen, Q., Tang, L., Hou, X., 2014. Toward a stepwise Kwangsian orogeny. Sci. China Earth Sci. 57, 379–387. https://doi.org/10.1007/s11430-013-4815-y.
Chen, X., Fan, J., Wang, W., Wang, H., Nie, H., Shi, X., Wen, Z., Chen, D., Li, W., 2017. Stage-progressive distribution pattern of the Lungmachi black graptolitic shales from Guizhou to Chongqing, Central China. Sci. China Earth Sci. 60, 1133–1146. https://doi.org/10.1007/s11430-016-9031-9.
Chen, X., Chen, Q., Zhen, Y., Wang, H., Zhang, L., Zhang, J., Wang, W., Xiao, Z., 2018. Circumjacent distribution pattern of the Lungmachian graptolitic black shale (early Silurian) on the Yichang Uplift and its peripheral region. Sci. China Earth Sci. 61, 1195–1203. https://doi.org/10.1007/s11430-017-9222-x.
Christ, N., Immenhauser, A., Amour, F., Mutti, M., Tomás, S., Agar, S., Alway, R., Kabiri, L., 2012. Characterization and Interpretation of Discontinuity Surfaces in a Jurassic Ramp Setting (High Atlas, Morocco). Sedimentology 59, 249–290. https://doi.org/10.1111/j.1365-3091.2011.01251.x.
Christ, N., Immenhauser, A., Wood, R.A., Darwich, K., Niedermayr, A., 2015. Petrography and environmental controls on the formation of Phanerozoic marine carbonate hardgrounds. Earth Sci. Rev. 151, 176–226. https://doi.org/10.1016/j.earscirev.2015.10.002.
Dashtgard, S.E., MacEachern, J.A., 2016. Unburrowed mudstones may record only slightly lowered oxygen conditions in warm, shallow basins. Geology 44 (5), 371–374. https://doi.org/10.1130/G37648.1.
de Boer, A.M., Sigman, D.M., Toggweiler, J.R., Russell, J.L., 2007. Effect of global ocean temperature change on deep ocean ventilation. Paleoceanography 22 (2), PA2210. https://doi.org/10.1029/2005PA001242.
de Castro, S., Hernández-Molina, F.J., de Weger, W., Jiménez-Espejo, F.J., Rodríguez-Tovar, F.J., Mena, A., Llave, E., Sierro, F.J., 2021. Contourite characterization and its discrimination from other deep-water deposits in the Gulf of Cadiz contourite depositional system. Sedimentology 68 (3), 987–1027. https://doi.org/10.1111/sed.12813.
DeReuil, A.A., Birgenheier, L.P., 2019. Sediment dispersal and organic carbon preservation in a dynamic mudstone-dominated system, Juana Lopez Member. Mancos Shale: Sedimentol. 66 (3), 1002–1041. https://doi.org/10.1111/sed.12532.
Ding, Z., Lu, R., Liu, X., Wu, Y., Chen, D., 2024. Geochemical evidence of provenance diversity in Holocene sandy land of Qinghai Lake Basin in the north-eastern margin of Qinghai–Tibet Plateau and its implications for climate change. Sedimentology 71 (1), 54–80. https://doi.org/10.1111/sed.13128.
Dutkiewicz, A., Müller, R.D., 2022. Deep-sea hiatuses track the vigor of Cenozoic Ocean bottom currents. Geology 50 (6), 710–715. https://doi.org/10.1130/G49810.1.
Dutkiewicz, A., Müller, R.D., Hogg, A.M., Spence, P., 2016. Vigorous deep-sea currents cause global anomaly in sediment accumulation in the Southern Ocean. Geology 44 (8), 663–666. https://doi.org/10.1130/G38143.1.
Elad, M., Gadol, O., Makovsky, Y., Almogi-Labin, A., Boaretto, E., Bookman, R., 2022. When did Goliath collapse? Dating the recent events of a major submarine slide complex, Southeastern Mediterranean margin. Sediment. Geol. 433, 106123. https://doi.org/10.1016/j.sedgeo.2022.106123.
Embry, A., 2009. Practical sequence stratigraphy. The Reservoir 36, 1–6. http://www.cspg.org.
Fang, Q., Wu, H., Wang, X., Yang, T., Li, H., Zhang, S., 2019. An astronomically forced cooling event during the Middle Ordovician. Glob. Planet. Chang. 173, 96–108. https://doi.org/10.1016/j.gloplacha.2018.12.010.
Farouk, S., Abdeldaim, A., Thibault, N., Aref, M., Elfiki, W., El-Kahtany, K., 2022. Cyclostratigraphy and eccentricity tunning of the middle Miocene succession, Gulf of Suez, Egypt: Astronomical age dating and undetected hiatus. Mar. Pet. Geol. 143, 105771. https://doi.org/10.1016/j.marpetgeo.2022.105771.
Föllmi, K.B., 2016. Sedimentary condensation. Earth Sci. Rev. 152, 143–180. https://doi.org/10.1016/j.earscirev.2015.11.016.
French, K.L., Flaum, J.A., Birdwell, J.E., 2024. An integrated perspective of paleoenvironmental change in the Western Interior Seaway before and during OAE-2 reveals how organic-rich mudstones form in dynamic environments. Earth Planet. Sci. Lett. 642, 118850. https://doi.org/10.1016/j.epsl.2024.118850.
Gambacorta, G., Trincianti, E., Torricelli, S., 2016. Anoxia controlled by relative sea-level changes: an example from the Mississippian Barnett Shale Formation. Palaeogeogr. Palaeoclimatol. Palaeoecol. 459, 306–320. https://doi.org/10.1016/j.palaeo.2016.07.015.
Gani, M.R., 2017. Mismatch between Time Surface and Stratal Surface in Stratigraphy. J. Sediment. Res. 87 (11), 1226–1234. https://doi.org/10.2110/jsr.2017.67.
Greene, J.A., Lizarralde, D., Tominaga, M., Tivey, M., 2020. Deep-ocean paleo-seafloor erosion in the northwestern Pacific identified by high-resolution seismic images. Mar. Geol. 429, 106330. https://doi.org/10.1016/j.margeo.2020.106330.
Hajek, E.A., Straub, K.M., 2017. Autogenic Sedimentation in Clastic Stratigraphy. Annu. Rev. Earth Planet. Sci. 45 (45), 681–709. https://doi.org/10.1146/annurev-earth-063016-015935.
Hall, I.R., McCave, I.N., Shackleton, N.J., Weedon, G.P., Harris, S.E., 2001. Intensified deep Pacific inflow and ventilation in Pleistocene glacial times. Nature 412 (6849), 809–812. https://doi.org/10.1038/35090552.
Hansen, M.A., Passchier, S., 2017. Oceanic circulation changes during early Pliocene marine ice-sheet instability in Wilkes Land, East Antarctica. Geo-Mar. Lett. 37 (3), 207–213. https://doi.org/10.1007/s00367-016-0489-8.
Haq, B.U., Schutter, S.R., 2008. A chronology of Paleozoic sea-level changes. Science 322 (5898), 64–68. https://doi.org/10.1126/science.1161648.
Harris, P.T., Whiteway, T., 2011. Global distribution of large submarine canyons: Geomorphic differences between active and passive continental margins. Mar. Geol. 285 (1), 69–86. https://doi.org/10.1016/j.margeo.2011.05.008.
Hemmesch, N.T., Harris, N.B., Mnich, C.A., Selby, D., 2014. A sequence-stratigraphic framework for the Upper Devonian Woodford Shale, Permian Basin, west Texas. AAPG Bull. 98 (1), 23–47. https://doi.org/10.1306/05221312077.
Hickey, J.J., Henk, B., 2007. Lithofacies summary of the Mississippian Barnett Shale, Mitchell 2 T.P. Sims well, Wise County, Texas. AAPG Bull. 91 (4), 437–443. https://doi.org/10.1306/12040606053.
Hilgen, F.J., Hinnov, L.A., Abdul Aziz, H., Abels, H.A., Batenburg, S., Bosmans, J.H., de Boer, B., Hüsing, S.K., Kuiper, K.F., Lourens, L.J., 2015. Stratigraphic continuity and fragmentary sedimentation: the success of cyclostratigraphy as part of integrated stratigraphy. In: Smith, D.G., Hinnov, L.A., Montenari, M. (Eds.), 2018, Chapter one - Cyclostratigraphy and Astrochronology in 2018, 3. Academic Press, pp. 1–80. Stratigraphy & Timescales.
Hillgaertner, H., 1998. Discontinuity surfaces on a shallow-marine carbonate platform (Berriasian, Valanginian, France and Switzerland). J. Sediment. Res. 68 (6), 1093–1108. https://doi.org/10.2110/jsr.68.1093.
Huang, H., Gao, Y., Ma, C., Niu, L., Dong, T., Tian, X., Cheng, H., Hei, C., Tao, H., Wang, C., 2021. Astronomical constraints on the development of alkaline lake during the Carboniferous-Permian Period in North Pangea. Glob. Planet. Chang. 207, 103681. https://doi.org/10.1016/j.gloplacha.2021.103681.
Immenhauser, A., Scott, R.W., 2002. An estimate of Albian Sea-level amplitudes and its implication for the duration of stratigraphic hiatuses. Sediment. Geol. 152 (1), 19–28. https://doi.org/10.1016/S0037-0738(02)00260-9.
Ineson, J.R., Lauridsen, B.W., Lode, S., Sheldon, E., Sørensen, H.O., Wisshak, M., Anderskouv, K., 2022. A condensed chalk–marl succession on an early cretaceous intrabasinal structural high, Danish Central Graben: Implications for the sequence stratigraphic interpretation of the Munk Marl Bed. Sediment. Geol. 440, 106234. https://doi.org/10.1016/j.sedgeo.2022.106234.
Ivanova, E., Borisov, D., Dmitrenko, O., Murdmaa, I., 2020. Hiatuses in the late Pliocene-Pleistocene stratigraphy of the Ioffe calcareous contourite drift, western South Atlantic. Mar. Pet. Geol. 111, 624–637. https://doi.org/10.1016/j.marpetgeo.2019.08.031.
Jin, S., Deng, H., Zhu, X., Liu, Y., Liu, S., Fu, M., 2020. Orbital control on cyclical organic matter accumulation in early Silurian Longmaxi Formation shales. Geosci. Front. 11 (2), 533–545. https://doi.org/10.1016/j.gsf.2019.06.005.
Jin, C., Liao, Z., Lash, G.G., 2021. High-frequency redox variation across the Ordovician-Silurian transition, South China. Palaeogeogr. Palaeoclimatol. Palaeoecol. 566, 110218. https://doi.org/10.1016/j.palaeo.2021.110218.
Johnson, D.A., 1974. Deep Pacific circulation: Intensification during the early Cenozoic. Mar. Geol. 17 (2), 71–78. https://doi.org/10.1016/0025-3227(74)90049-8.
Johnson, M.E., 2010. Tracking Silurian eustasy: Alignment of empirical evidence or pursuit of deductive reasoning? Palaeogeogr. Palaeoclimatol. Palaeoecol. 296 (3), 276–284. https://doi.org/10.1016/j.palaeo.2009.11.024.
Kabanov, P., 2017. Stratigraphic unconformities: Review of the concept and examples from the Middle-Upper Paleozoic. In: Aiello, G. (Ed.), Seismic and Sequence Stratigraphy and Integrated Stratigraphy - New Insights and Contributions. BoD–Books on Demand, London, UK, pp. 101–127. https://doi.org/10.5772/intechopen.70373.
Kemp, D.B., Fraser, W.T., Izumi, K., 2018. Stratigraphic completeness and resolution in an ancient mudrock succession. Sedimentology 65 (6), 1875–1890. https://doi.org/10.1111/sed.12450.
Kennett, J., Watkins, N., 1975. Deep-sea erosion and manganese nodule development in the Southeast Indian Ocean. Science 188 (4192), 1011–1013. https://doi.org/10.1126/science.188.4192.1011.
Laskar, J., 2008. Chaotic diffusion in the Solar System. Icarus 196 (1), 1–15. https://doi.org/10.1016/j.icarus.2008.02.017.
Lazar, O.R., Bohacs, K.M., Macquaker, J.H., Schieber, J., Demko, T.M., 2015a. Capturing key attributes of fine-grained sedimentary rocks in outcrops, cores, and thin sections: nomenclature and description guidelines. J. Sediment. Res. 85 (3), 230–246. https://doi.org/10.2110/jsr.2015.11.
Lazar, O.R., Bohacs, K.M., Schieber, J., Macquaker, J.H., Demko, T.M., 2015b. Mud-stone Primer: Lithofacies variations, diagnostic criteria, and sedimentologic-stratigraphic implications at lamina to bedset scale. In: SEPM Society for Sedimentary Geology

ed., Sepm Concepts in Sedimentology and Paleontology, 12. SEPM Society for Sedimentary Geology. https://doi.org/10.2110/sepmcsp.12.
Li, Y., Schieber, J., Fan, T., Li, Z., Zhang, J., 2017a. Regional depositional changes and their controls on carbon and sulfur cycling across the Ordovician-Silurian boundary, northwestern Guizhou, South China. Palaeogeogr. Palaeoclimatol. Palaeoecol. 485, 816–832. https://doi.org/10.1016/j.palaeo.2017.07.039.
Li, Y., Zhang, T., Ellis, G.S., Shao, D., 2017b. Depositional environment and organic matter accumulation of Upper Ordovician–Lower Silurian marine shale in the Upper Yangtze Platform, South China. Palaeogeogr. Palaeoclimatol. Palaeoecol. 466, 252–264. https://doi.org/10.1016/j.palaeo.2016.11.037.
Li, M., Huang, C., Hinnov, L., Ogg, J., Chen, Z.-Q., Zhang, Y., 2016. Obliquity-forced climate during the early Triassic hothouse in China. Geology 44 (8), 623–626. https://doi.org/10.1130/G37970.1.
Li, M., Hinnov, L.A., Huang, C., Ogg, J.G., 2018a. Sedimentary noise and sea levels linked to land-ocean water exchange and obliquity forcing. Nat. Commun. 9 (1), 1004. https://doi.org/10.1038/s41467-018-03454-y.
Li, M., Kump, L.R., Hinnov, L.A., Mann, M.E., 2018b. Tracking variable sedimentation rates and astronomical forcing in Phanerozoic paleoclimate proxy series with evolutionary correlation coefficients and hypothesis testing. Earth Planet. Sci. Lett. 501, 165–179. https://doi.org/10.1016/j.epsl.2018.08.041.
Li, M., Hinnov, L., Kump, L., 2019. Acycle: Time-series analysis software for paleoclimate research and education. Comput. Geosci. 127, 12–22. https://doi.org/10.1016/j.cageo.2019.02.011.
Li, S., Zhou, Z., Nie, H., Liu, M., Meng, F., Shen, B., Zhang, X., Wei, S., Xi, Z., Zhang, S., 2023. Organic matter accumulation mechanisms in the Wufeng-Longmaxi shales in western Hubei Province, China and paleogeographic implications for the uplift of the Hunan-Hubei Submarine high. Int. J. Coal Geol. 270, 104223. https://doi.org/10.1016/j.coal.2023.104223.
Li, R., Zhou, X., Eddy, M.P., Ickert, R.B., Wang, Z., Tang, D., Huang, K.-J., Peng, P., 2024. Stratigraphic evidence for a major unconformity within the Ediacaran System. Earth Planet. Sci. Lett. 636, 118715. https://doi.org/10.1016/j.epsl.2024.118715.
Liang, C., Jiang, Z., Yang, Y., Wei, X., 2012. Shale lithofacies and reservoir space of the Wufeng-Longmaxi Formation, Sichuan Basin, China. Pet. Explor. Dev. 39 (6), 736–743. https://doi.org/10.1016/S1876-3804(12)60098-6.
Liang, C., Jiang, Z., Cao, Y., Wu, M., Guo, L., Zhang, C., 2016. Deep-water depositional mechanisms and significance for unconventional hydrocarbon exploration: a case study from the lower Silurian Longmaxi shale in the southeastern Sichuan Basin. AAPG Bull. 100 (5), 773–794. https://doi.org/10.1306/02031615002.
Liu, Z., Algeo, T.J., Guo, X., Fan, J., Du, X., Lu, Y., 2017. Paleo-environmental cyclicity in the early Silurian Yangtze Sea (South China): Tectonic or glacio-eustatic control? Palaeogeogr. Palaeoclimatol. Palaeoecol. 466, 59–76. https://doi.org/10.1016/j.palaeo.2016.11.007.
Liu, S., Yang, Y., Deng, B., Zhong, Y., Wen, L., Sun, W., Li, Z., Jansa, L., Li, J., Song, J., Zhang, X., Peng, H., 2021. Tectonic evolution of the Sichuan Basin, Southwest China. Earth Sci. Rev. 213, 103470. https://doi.org/10.1016/j.earscirev.2020.103470.
Loucks, R.G., Ruppel, S.C., 2007. Mississippian Barnett Shale: Lithofacies and depositional setting of a deep-water shale-gas succession in the Fort Worth Basin, Texas. AAPG Bull. 91 (4), 579–601. https://doi.org/10.1306/11020606059.
Loydell, D.K., 2007. Early Silurian positive δ13C excursions and their relationship to glaciations, sea-level changes and extinction events. Geol. J. 42 (5), 531–546. https://doi.org/10.1002/gj.1090.
Lu, Y., Hao, F., Lu, Y., Yan, D., Xu, S., Shu, Z., Wang, Y., Wu, L., 2020. Lithofacies and depositional mechanisms of the Ordovician-Silurian Wufeng-Longmaxi organic-rich shales in the Upper Yangtze area, southern China. AAPG Bull. 104 (1), 97–129. https://doi.org/10.1306/04301918099.
Lu, Y., Yue, Y., Lu, Y., Jiang, S., Wang, Y., 2023. Sedimentary response to the early Silurian (Rhuddanian-Aeronian) post-glacial transgression and Kwangsian Orogeny in the Upper Yangtze region, South China. Palaeogeogr. Palaeoclimatol. Palaeoecol. 623, 111639. https://doi.org/10.1016/j.palaeo.2023.111639.
Macquaker, J.H., Bohacs, K.M., 2008. On the accumulation of mud. Science 318 (5857), 1734–1735. https://doi.org/10.1126/science.1151980.
Macquaker, J.H., Taylor, K.G., Gawthorpe, R.L., 2007. High-resolution facies analyses of mudstones: implications for paleoenvironmental and sequence stratigraphic interpretations of offshore ancient mud-dominated successions. J. Sediment. Res. 77 (4), 324–339. https://doi.org/10.2110/jsr.2007.029.
Macquaker, J.H., Bentley, S.J., Bohacs, K.M., 2010. Wave-enhanced sediment-gravity flows and mud dispersal across continental shelves: Reappraising sediment transport processes operating in ancient mudstone successions. Geology 38 (10), 947–950. https://doi.org/10.1130/G31093.1.
Mann, M.E., Lees, J.M., 1996. Robust estimation of background noise and signal detection in climatic time series. Clim. Chang. 33 (3), 409–445. https://doi.org/10.1007/BF00142586.
März, C., Vogt, C., Schnetger, B., Brumsack, H.-J., 2011. Variable Eocene-Miocene sedimentation processes and bottom water redox conditions in the Central Arctic Ocean (IODP Expedition 302). Earth Planet. Sci. Lett. 310 (3), 526–537. https://doi.org/10.1016/j.epsl.2011.08.025.
McLaughlin, P., Brett, C., Wilson, M., 2008. Hierarchy of sedimentary discontinuity surfaces and condensed beds from the middle Paleozoic of eastern North America: Implications for cratonic sequence stratigraphy. In: Pratt and Holmden, ed., Special Paper 48: Dynamics of Epeiric Seas: Special Paper-Geological Association of Canada, pp. 175–200.
Melchin, M.J., Holmden, C., 2006. Carbon isotope chemostratigraphy of the Llandovery in Arctic Canada: implications for global correlation and sea-level change. Gff 128 (2), 173–180. https://doi.org/10.1080/11035890601282173.
Melchin, M.J., Sadler, P.M., Cramer, B.D., 2020. Chapter 21 - the Silurian Period. In: Gradstein, F.M., Ogg, J.G., Schmitz, M.D., Ogg, G.M. (Eds.), Geologic Time Scale 2020. Elsevier, pp. 695–732.
Meyers, S.R., Sageman, B.B., 2004. Detection, quantification, and significance of hiatuses in pelagic and hemipelagic strata. Earth Planet. Sci. Lett. 224 (1), 55–72. https://doi.org/10.1016/j.epsl.2004.05.003.
Meyers, S.R., Sageman, B.B., Hinnov, L.A., 2001. Integrated Quantitative Stratigraphy of the Cenomanian-Turonian Bridge Creek Limestone Member using Evolutive Harmonic Analysis and Stratigraphic Modeling. J. Sediment. Res. 71 (4), 628–644. https://doi.org/10.1306/012401710628.
Miall, A.D., 2015. Updating uniformitarianism: stratigraphy as just a set of 'frozen accidents': Geological Society, London. Special Publications 404 (1), 11–36. https://doi.org/10.1144/SP404.4.
Miall, A.D., 2016. The valuation of unconformities. Earth Sci. Rev. 163, 22–71. https://doi.org/10.1016/j.earscirev.2016.09.011.
Moore Jr., T., Van Andel, T.H., Sancetta, C., Pisias, N., 1978. Cenozoic hiatuses in pelagic sediments. Micropaleontology 113–138. https://doi.org/10.2307/1485246.
Moshe, N., Katz, O., Torfstein, A., Kanari, M., Masque, P., Hyams-Kaphzan, O., 2024. Glacial-Holocene variability in sediment accumulation and erosion along submarine blind canyons: a case study from Eastern Mediterranean Sea. Mar. Geol. 469, 107217. https://doi.org/10.1016/j.margeo.2024.107217.
Mulder, T., Syvitski, J.P., 1995. Turbidity currents generated at river mouths during exceptional discharges to the world oceans. J. Geol. 103 (3), 285–299. https://doi.org/10.1086/629747.
Munnecke, A., Calner, M., Harper, D.A.T., Servais, T., 2010. Ordovician and Silurian Sea–water chemistry, sea level, and climate: a synopsis. Palaeogeogr. Palaeoclimatol. Palaeoecol. 296 (3), 389–413. https://doi.org/10.1016/j.palaeo.2010.08.001.
Nesbitt, H.W., Young, G.M., 1982. Early Proterozoic climates and plate motions inferred from major element chemistry of lutites. Nature 299 (5885), 715–717. https://doi.org/10.1038/299715a0.
Nie, Y., Wu, H., Satolli, S., Ferré, E.C., Shi, M., Fang, Q., Xu, Y., Zhang, S., Li, H., Yang, T., 2023. Late Miocene to present Paleoclimatic and Paleoenvironmental Evolution of the South China Sea Recorded in the Magneto-Cyclostratigraphy of IODP Site U1505. Paleoceanog. Paleoclimatol. 38 (2), e2022PA004547. https://doi.org/10.1029/2022PA004547.
Nie, H., Li, P., Chen, Q., Jin, Z., Liu, Q., Dang, W., Chen, Q., Ding, J., Zhai, C., 2024. A world-class source rock in southern China formed during the periods from Katian to Rhuddanian: Biostratigraphic distribution, depositional model and shale gas potential. Gondwana Res. 126, 267–288. https://doi.org/10.1016/j.gr.2023.10.007.
Nordsvan, A.R., Bauer, K.W., Colleps, C.L., Mitchell, R.N., McKenzie, N.R., 2025. Modeling the stratigraphic record of glacioeustatic sea-level rise and sediment starvation following Snowball Earth. Earth Planet. Sci. Lett. 659, 119332. https://doi.org/10.1016/j.epsl.2025.119332.
Nugraha, H.D., Jackson, C.A.-L., Johnson, H.D., Hodgson, D.M., Clare, M.A., 2022. Extreme erosion by submarine slides. Geology 50 (10), 1130–1134. https://doi.org/10.1130/G50164.1.
Olde, K., Jarvis, I., Uličný, D., Pearce, M.A., Trabucho-Alexandre, J., Čech, S., Gröcke, D. R., Laurin, J., Švábenická, L., Tocher, B.A., 2015. Geochemical and palynological sea-level proxies in hemipelagic sediments: a critical assessment from the Upper cretaceous of the Czech Republic. Palaeogeogr. Palaeoclimatol. Palaeoecol. 435, 222–243. https://doi.org/10.1016/j.palaeo.2015.06.018.
Ondřej, B., Martin, F., Daniel, Š., Hedvika, W., Jindřich, H., Jiří, K., 2018. Sea-Level Changes Vs. Organic Productivity as Controls on Early and Middle Devonian Bioevents: Facies- and Gamma-Ray Based Sequence-Stratigraphic Correlation of the Prague Basin. Global and Planetary Change, Czech Republic. https://doi.org/10.1016/j.gloplacha.2017.11.009.
Ou, C., Li, C., Rui, Z., Ma, Q., 2018. Lithofacies distribution and gas-controlling characteristics of the Wufeng-Longmaxi black shales in the southeastern region of the Sichuan Basin, China. J. Pet. Sci. Eng. 165, 269–283. https://doi.org/10.1016/j.petrol.2018.02.024.
Paola, C., Ganti, V., Mohrig, D., Runkel, A.C., Straub, K.M., 2018. Time not our time: physical controls on the preservation and measurement of geologic time. Annu. Rev. Earth Planet. Sci. 46 (1), 409–438. https://doi.org/10.1146/annurev-earth-082517-010129.
Paz, M., Buatois, L.A., Mángano, M.G., Desjardins, P.R., Notta, R., González Tomassini, F., Carmona, N.B., Minisini, D., 2022. Organic-rich, fine-grained contourites in an epicontinental basin: the Upper Jurassic-lower cretaceous Vaca Muerta Formation, Argentina. Mar. Pet. Geol. 142, 105757. https://doi.org/10.1016/j.marpetgeo.2022.105757.
Plantz, J.B., Sedorko, D., Carelli, T.G., Ramos, R.R.C., Borghi, L., 2024. Depositional processes in a shale-dominated Devonian succession: Sedimentary facies and trace fossil integrated analysis. Sediment. Geol. 470, 106716. https://doi.org/10.1016/j.sedgeo.2024.106716.
Potter, P.E., Maynard, J.B., Depetris, P.J., 2005. Mud and Mudstones: Introduction and Overview. Springer Science & Business Media, Berlin, pp. 1–297.
Puga-Bernabéu, Á., Betzler, C., 2008. Cyclicity in Pleistocene upper-slope cool-water carbonates: Unravelling sedimentary dynamics in deep-water sediments, Great Australian Bight, Odp Leg 182, Site 1131A. Sediment. Geol. 205 (1), 40–52. https://doi.org/10.1016/j.sedgeo.2008.01.008.
Qiu, Z., Liu, B., Lu, B., Shi, Z., Li, Z., 2022. Mineralogical and petrographic characteristics of the Ordovician-Silurian Wufeng-Longmaxi Shale in the Sichuan Basin and implications for depositional conditions and diagenesis of black shales. Mar. Pet. Geol. 135, 105428. https://doi.org/10.1016/j.marpetgeo.2021.105428.

Radley, J.D., 2008. Seafloor erosion and sea-level change: early Jurassic Blue Lias Formation of Central England. Palaeogeogr. Palaeoclimatol. Palaeoecol. 270 (3), 287–294. https://doi.org/10.1016/j.palaeo.2008.01.029.
Rodríguez-Tovar, F.J., 2022. Ichnological analysis: a tool to characterize deep-marine processes and sediments. Earth Sci. Rev. 228, 104014. https://doi.org/10.1016/j.earscirev.2022.104014.
Ruffell, A., Worden, R., 2000. Palaeoclimate analysis using spectral gamma-ray data from the Aptian (cretaceous) of southern England and southern France. Palaeogeogr. Palaeoclimatol. Palaeoecol. 155 (3), 265–283. https://doi.org/10.1016/S0031-0182(99)00119-4.
Sadler, P.M., 1999. The Influence of Hiatuses on Sediment Accumulation Rates. In: Bruns, P., Haas, H.C. (Eds.), On the Determination of Sediment Accumulation Rates: GeoResearch Forum, 5. Trans Tech Publications, pp. 15–40. doi: 10013/epic.14855.
Sageman, B.B., Murphy, A.E., Werne, J.P., Ver Straeten, C.A., Hollander, D.J., Lyons, T. W., 2003. A tale of shales: the relative roles of production, decomposition, and dilution in the accumulation of organic-rich strata, Middle–Upper Devonian, Appalachian basin. Chem. Geol. 195 (1), 229–273. https://doi.org/10.1016/S0009-2541(02)00397-2.
Salazar, S., Castillo, L.A., Montes, L., 2023. Definition of unconformities based on radiometric tool. Appl. Radiat. Isot. 199, 110872. https://doi.org/10.1016/j.apradiso.2023.110872.
Sattler, U., Immenhauser, A., Hillgärtner, H., Esteban, M., 2005. Characterization, lateral variability and lateral extent of discontinuity surfaces on a Carbonate Platform (Barremian to lower Aptian, Oman). Sedimentology 52 (2), 339–361. https://doi.org/10.1111/j.1365-3091.2005.00701.x.
Schieber, J., 1994. Evidence for high-energy events and shallow-water deposition in the Chattanooga Shale, Devonian, central Tennessee, USA. Sediment. Geol. 93 (3), 193–208. https://doi.org/10.1016/0037-0738(94)90005-1.
Schieber, J., 2003. Simple gifts and buried treasures–implications of finding bioturbation and erosion surfaces in black shales: the Sedimentary. Record 1 (2), 4–8. https://doi.org/10.2110/sedred.2003.2.4.
Schieber, J., 2016. Mud re-distribution in epicontinental basins-Exploring likely processes. Mar. Pet. Geol. 71, 119–133. https://doi.org/10.1016/j.marpetgeo.2015.12.014.
Schieber, J., Baird, G., 2001. On the origin and significance of pyrite spheres in Devonian black shales of North America. J. Sediment. Res. 71 (1), 155–166. https://doi.org/10.1306/051600710155.
Schieber, J.R., Riciputi, L., 2004. Pyrite ooids in Devonian black shales record intermittent sea-level drop and shallow-water conditions. Geology 32 (4), 305–308. https://doi.org/10.1130/G20202.1.
Schieber, J., Shao, X., 2021. Detecting detrital carbonate in shale successions - Relevance for evaluation of depositional setting and sequence stratigraphic interpretation. Mar. Pet. Geol. 130, 105130. https://doi.org/10.1016/j.marpetgeo.2021.105130.
Schieber, J., Southard, J.B., 2009. Bedload transport of mud by floccule ripples—Direct observation of ripple migration processes and their implications. Geology 37 (6), 483–486. https://doi.org/10.1130/G25319A.1.
Schieber, J., Southard, J., Thaisen, K., 2007. Accretion of Mudstone Beds from Migrating Floccule ripples. Science 318 (5857), 1760–1763. https://doi.org/10.1126/science.1147001.
Schieber, J., Southard, J.B., Schimmelmann, A., 2010. Lenticular shale fabrics resulting from intermittent erosion of water-rich muds—interpreting the rock record in the light of recent flume experiments. J. Sediment. Res. 80 (1), 119–128. https://doi.org/10.2110/jsr.2010.005.
Schimmelmann, A., Lange, C.B., Schieber, J., Francus, P., Ojala, A.E.K., Zolitschka, B., 2016. Varves in marine sediments: a review. Earth Sci. Rev. 159, 215–246. https://doi.org/10.1016/j.earscirev.2016.04.009.
Schnyder, J., Ruffell, A., Deconinck, J.-F., Baudin, F., 2006. Conjunctive use of spectral gamma-ray logs and clay mineralogy in defining late Jurassic–early cretaceous palaeoclimate change (Dorset, U.K.). Palaeogeogr. Palaeoclimatol. Palaeoecol. 229 (4), 303–320. https://doi.org/10.1016/S0031-0182(99)00119-4.
Shen, J., Wang, P., Chen, K., Zhang, D., Wang, Y., Cai, Q., Meng, J., 2021. Relationship between volcanic activity and enrichment of shale organic matter during the Ordovician-Silurian transition in western Hubei, Southern China. Palaeogeogr. Palaeoclimatol. Palaeoecol. 577, 110551. https://doi.org/10.1016/j.palaeo.2021.110551.
Smith, D.G., Bailey, R.J., Burgess, P.M., Fraser, A.J., 2015. Strata and time: probing the gaps in our understanding: Geological Society. London, Special Publications 404 (1), 1–10. https://doi.org/10.1144/SP404.16.
Sommerfield, C.K., 2006. On sediment accumulation rates and stratigraphic completeness: Lessons from Holocene Ocean margins. Cont. Shelf Res. 26 (17), 2225–2240. https://doi.org/10.1016/j.csr.2006.07.015.
Storch, P., Frýda, J., 2012. Late Aeronian graptolite *sedgwickii* event, associated carbon isotope excursion and facies changes in the Prague Synform (Barrandian, Bohemia). Geol. Mag. 149, 1089–1106. https://doi.org/10.1017/S001675681200026X.
Stow, D., Smillie, Z., 2020. Distinguishing between deep-water sediment facies: turbidites, contourites and hemipelagites. Geosciences 10 (2), 68. https://doi.org/10.3390/geosciences10020068.
Stow, D.A.V., Huc, A.Y., Bertrand, P., 2001. Depositional processes of black shales in deep water. Mar. Pet. Geol. 18 (4), 491–498. https://doi.org/10.1016/S0264-8172(01)00012-5.
Strasser, A., 2015. Hiatuses and condensation: an estimation of time lost on a shallow carbonate platform: the Depositional. Record 1 (2), 91–117. https://doi.org/10.1002/dep2.9.
Tagliaro, G., Fulthorpe, C.S., Watkins, D.K., De Vleeschouwer, D., Brumsack, H., Bogus, K., Lavier, L.L., 2022. Late Miocene-Pliocene vigorous deep-sea circulation in the Southeast Indian Ocean: Paleoceanographic and tectonic implications. Paleoceanog. Paleoclimatol. 37 (1), e2021PA004303. https://doi.org/10.1029/2021PA004303.
Thomas, N.C., Bradbury, H.J., Hodell, D.A., 2022. Changes in North Atlantic deep-water oxygenation across the Middle Pleistocene transition. Science 377 (6606), 654–659. https://doi.org/10.1126/science.abj7761.
Thomson, D.J., 1982. Spectrum estimation and harmonic analysis. Proc. IEEE 70 (9), 1055–1096. https://doi.org/10.1109/PROC.1982.12433.
Thomson, D.J., 1990. Time series analysis of Holocene climate data: Philosophical transactions of the Royal Society of London. Series A, Mathemat. Phys. Sci. 330 (1615), 601–616. https://doi.org/10.1098/rsta.1990.0041.
Tomer, A., Muto, T., Kim, W., 2011. Autogenic hiatus in fluviodeltaic successions: geometrical modeling and physical experiments. J. Sediment. Res. 81 (3), 207–217. https://doi.org/10.2110/jsr.2011.19.
Trabucho-Alexandre, J., 2015. More gaps than shale: Erosion of mud and its effect on preserved geochemical and palaeobiological signals: Geological Society. London, Special Publications 404 (1), 251–270. https://doi.org/10.1144/SP404.10.
Tribovillard, N., Algeo, T.J., Lyons, T., Riboulleau, A., 2006. Trace metals as paleoredox and paleoproductivity proxies: an update. Chem. Geol. 232 (1), 12–32. https://doi.org/10.1016/j.chemgeo.2006.02.012.
Tribovillard, N., Algeo, T.J., Baudin, F., Riboulleau, A., 2012. Analysis of marine environmental conditions based onmolybdenum–uranium covariation—applications to Mesozoic paleoceanography. Chem. Geol. 324-325, 46–58. https://doi.org/10.1016/j.chemgeo.2011.09.009.
Trotter, J.A., Williams, I.S., Barnes, C.R., Männik, P., Simpson, A., 2016. New conodont δ18O records of Silurian climate change: Implications for environmental and biological events. Palaeogeogr. Palaeoclimatol. Palaeoecol. 443, 34–48. https://doi.org/10.1016/j.palaeo.2015.11.011.
Vahlenkamp, M., Niezgodzki, I., De Vleeschouwer, D., Lohmann, G., Bickert, T., Pälike, H., 2018. Ocean and climate response to North Atlantic seaway changes at the onset of long-term Eocene cooling. Earth Planet. Sci. Lett. 498, 185–195. https://doi.org/10.1016/j.epsl.2018.06.031.
van der Merwe, W.C., Flint, S.S., Hodgson, D.M., 2010. Sequence stratigraphy of an argillaceous, Deepwater basin-plain succession: Vischkuil Formation (Permian), Karoo Basin, South Africa. Mar. Pet. Geol. 27 (2), 321–333. https://doi.org/10.1016/j.marpetgeo.2009.10.007.
von der Heydt, A.S., Ashwin, P., Camp, C.D., Crucifix, M., Dijkstra, H.A., Ditlevsen, P., Lenton, T.M., 2021. Quantification and interpretation of the climate variability record. Glob. Planet. Chang. 197, 103399. https://doi.org/10.1016/j.gloplacha.2020.103399.
Waltham, D., 2015. Milankovitch period uncertainties and their impact on cyclostratigraphy. J. Sediment. Res. 85 (8), 990–998. https://doi.org/10.2110/jsr.2015.66.
Wang, C., Zhang, B., Hu, Q., Shu, Z., Sun, M., Bao, H., 2019a. Laminae characteristics and influence on shale gas reservoir quality of lower Silurian Longmaxi Formation in the Jiaoshiba area of the Sichuan Basin, China. Mar. Pet. Geol. 109, 839–851. https://doi.org/10.1016/j.marpetgeo.2019.06.022.
Wang, Y., Xu, S., Hao, F., Lu, Y., Shu, Z., Yan, Detian, Lu, Y., 2019b. Geochemical and petrographic characteristics of Wufeng-Longmaxi shales, Jiaoshiba area, Southwest China: Implications for organic matter differential accumulation. Mar. Pet. Geol. 102, 138–154. https://doi.org/10.1016/j.marpetgeo.2018.12.038.
Wang, M., Li, M., Kemp, D.B., Landwehrs, J., Jin, Z., 2023a. Late Triassic sedimentary records reveal the hydrological response to climate forcing and the history of the chaotic Solar System. Earth Planet. Sci. Lett. 607, 118052. https://doi.org/10.1016/j.epsl.2023.118052.
Wang, H., Shi, Z., Sun, S., Zhao, Q., Zhou, T., Cheng, F., Bai, W., 2023b. Microfacies types and distribution of epicontinental shale: A case study of the Wufeng–Longmaxi Shale in Southern sichuan basin, China. Pet. Explor. Dev. 50 (1), 57–71. https://doi.org/10.1016/S1876-3804(22)60369-0.
Wang, M., Li, M., Hajek, E.A., Kemp, D.B., Wu, Y., Zhu, H., Huang, C., Zhang, H., Ji, K., Zhang, R., Wei, R., Jin, Z., 2024. Assessing the preservation of orbital signals across different sedimentary environments: Insights from stochastic sedimentation modeling. Earth Planet. Sci. Lett. 642, 118866. https://doi.org/10.1016/j.epsl.2024.118866.
Weedon, G.P., 2003. Time-Series Analysis and Cyclostratigraphy: Examining Stratigraphic Records of Environmental Cycles. Cambridge University Press, Cambridge. https://doi.org/10.1017/CBO9780511535482.
Wei, R., Li, M., Zhang, R., Hu, Y., Ogg, J.G., Liu, G., Huang, H., He, X., Yuan, S., Lin, Q., Jin, Z., 2023. Obliquity forcing of continental aquifers during the late Paleozoic ice age. Earth Planet. Sci. Lett. 613, 118174. https://doi.org/10.1016/j.epsl.2023.118174.
Wheeler, H.E., 1964. Baselevel, Lithosphere Surface, and Time-Stratigraphy. GSA Bull. 75 (7), 599–610. https://doi.org/10.1130/0016-7606(1964)75[599:BLSAT]2.0.CO;2.
Wilson, R.D., Schieber, J., 2014. Muddy prodeltaic hyperpycnites in the lower Genesee Group of Central New York, USA: Implications for mud transport in epicontinental seas. J. Sediment. Res. 84 (10), 866–874. https://doi.org/10.2110/jsr.2014.70.
Wilson, R.D., Schieber, J., 2015. Sedimentary facies and depositional environment of the Middle Devonian Geneseo Formation of New York, USA. J. Sediment. Res. 85 (11), 1393–1415. https://doi.org/10.2110/jsr.2015.88.
Wroblewski, A.F.J., Morris, E.A., 2023. Unconformity generation and the shift from storm-dominated to tide-dominated processes in a Jurassic retroarc foreland basin: Insights from ichnology. Depositional Rec. 9 (2), 253–299. https://doi.org/10.1002/dep2.215.
Wu, H., Fang, Q., Hinnov, L.A., Zhang, S., Yang, T., Shi, M., Li, H., 2023. Astronomical time scale for the Paleozoic Era. Earth Sci. Rev. 244, 104510. https://doi.org/10.1016/j.earscirev.2023.104510.

Xu, C., Jia-yu, R., Yue, L., Boucot, A.J., 2004. Facies patterns and geography of the Yangtze region, South China, through the Ordovician and Silurian transition. Palaeogeogr. Palaeoclimatol. Palaeoecol. 204 (3), 353–372. https://doi.org/10.1016/S0031-0182(03)00736-3.

Xu, Y.-J., Cawood, P.A., Du, Y.-S., 2016. Intraplate orogenesis in response to Gondwana assembly: Kwangsian Orogeny, South China. Am. J. Sci. 316 (4), 329–362. https://doi.org/10.2475/04.2016.02.

Yang, T., Liu, Y.-L., 2025. New progresses of fine-grained sediment gravity-flow deposits and their importance for unconventional shale oil and gas plays. Pet. Sci. 22 (1), 1–15. https://doi.org/10.1016/j.petsci.2024.05.022.

Yang, S., Hu, W., Wang, X., Jiang, B., Yao, S., Sun, F., Huang, Z., Zhu, F., 2019. Duration, evolution, and implications of volcanic activity across the Ordovician-Silurian transition in the lower Yangtze region, South China. Earth Planet. Sci. Lett. 518, 13–25. https://doi.org/10.1016/j.epsl.2019.04.020.

Yang, S., Hu, W., Yao, S., Wang, X., He, W., Wang, Y., Zhu, F., Sun, F., 2020. Constraints on the accumulation of organic matter in Upper Ordovician-lower Silurian black shales from the lower Yangtze region, South China. Mar. Pet. Geol. 120, 104544. https://doi.org/10.1016/j.marpetgeo.2020.104544.

Yang, X., Yan, D., Zhang, B., Zhang, L., Wei, X., Li, T., Zhang, J., She, X., 2021. The impact of volcanic activity on the deposition of organic-rich shales: evidence from carbon isotope and geochemical compositions. Mar. Pet. Geol. 128, 105010. https://doi.org/10.1016/j.marpetgeo.2021.105010.

Yang, T., Sun, H., Cao, Y., Luo, C., Dodd, T.J.H., 2024. Gravel-inlaid mud clasts as indicators of transport processes of subaqueous sediment gravity-flows. Sediment. Geol. 472, 106741. https://doi.org/10.1016/j.sedgeo.2024.106741.

Yawar, Z., Schieber, J., 2017. On the origin of silt laminae in laminated shales. Sediment. Geol. 360, 22–34. https://doi.org/10.1016/j.sedgeo.2017.09.001.

Zavala, C., Arcuri, M., 2016. Intrabasinal and extrabasinal turbidites: Origin and distinctive characteristics. Sediment. Geol. 337, 36–54. https://doi.org/10.1016/j.sedgeo.2016.03.008.

Zeebe, R.E., Kocken, I.J., 2024. Applying astronomical solutions and Milanković forcing in the Earth sciences. Earth Sci. Rev., 104959 https://doi.org/10.1016/j.earscirev.2024.104959.

Zeeden, C., Laskar, J., De Vleeschouwer, D., Pas, D., Da Silva, A.-C.J.E., Letters, P.S., 2023. Earth's rotation and Earth-Moon distance in the Devonian derived from multiple geological records. Earth Planet. Sci. Lett. 621, 118348. https://doi.org/10.1016/j.epsl.2023.118348.

Zeller, M., Verwer, K., Eberli, G.P., Massaferro, J.L., Schwarz, E., Spalletti, L., 2015. Depositional controls on mixed carbonate–siliciclastic cycles and sequences on gently inclined shelf profiles. Sedimentology 62 (7), 2009–2037. https://doi.org/10.1111/sed.12215.

Zhang, T., Li, Y., Fan, T., Da Silva, A.-C., Shi, J., Gao, Q., Kuang, M., Liu, W., Gao, Z., Li, M., 2022. Orbitally-paced climate change in the early Cambrian and its implications for the history of the Solar System. Earth Planet. Sci. Lett. 583, 117420. https://doi.org/10.1016/j.epsl.2022.117420.

Zhang, R., Kemp, D.B., Thibault, N., Jelby, M.E., Li, M., Huang, C., Sui, Y., Wang, Z., Liu, D., Jia, S., 2023a. Astrochronology and sedimentary noise modeling of Pliensbachian (early Jurassic) sea-level changes, Paris Basin, France. Earth Planet. Sci. Lett. 614, 118199. https://doi.org/10.1016/j.epsl.2023.118199.

Zhang, Q., Swann, G.E.A., Liu, J., Gao, W., Cui, Z., Li, G., Zhao, X., Li, W., 2023b. Sea level controls on the provenance of fine-grained sediments in the Xisha Trough, northwestern South China Sea over the last ~30 ka. Mar. Geol. 466, 107184. https://doi.org/10.1016/j.margeo.2023.107184.

Zhao, J., Jin, Z., Jin, Z., Geng, Y., Wen, X., Yan, C., 2016. Applying sedimentary geochemical proxies for paleoenvironment interpretation of organic-rich shale deposition in the Sichuan Basin, China. Int. J. Coal Geol. 163, 52–71. https://doi.org/10.1016/j.coal.2016.06.015.